Widespread fault creep in the northern San Francisco Bay Area revealed by multi-station cluster detection of repeating earthquakes

Nader Shakibay Senobari[1,2], **Gareth J. Funning**[1]

[1]Department of Earth and Planetary Sciences, University of California, Riverside, CA
[2]Now at Department of Computer Science and Engineering, University of California, Riverside, CA

Key Points:

- We identify 59 repeating earthquake families, each validated by double-difference relocation
- Multi-station clustering allows us to detect repeating earthquakes despite a changing seismic network
- Repeating earthquakes are clustered on three major faults, and imply widespread aseismic creep

Corresponding author: Nader Shakibay Senobari, nshak006@ucr.edu

Abstract
We search for repeating earthquakes (REs) in the northern San Francisco Bay Area in 1984–2016. By comparing over 670,000 waveforms from ~ 75,000 events, we identify candidate clusters of events whose waveforms have high cross-correlation coefficients at multiple stations. A key difference with our approach is that these 'multi-station clusters' do not require each event in a family be recorded at multiple common stations. We validate these candidate REs by estimating precise relative relocations for the events in each cluster.

We identify 59 RE families whose relocated hypocenters are separated by less than one source radius. These are distributed throughout the Maacama fault zone, and along the northern Rodgers Creek and central Bartlett Springs faults, implying that widespread, pervasive creep occurs on those faults, at rates of 1–6 mm/yr. At either end of the Maacama fault, the RE pattern highlights structural complexity, suggesting that multiple subparallel strands may be active and creeping.

Plain language summary
Repeating earthquakes (REs) are small earthquakes that repeat in the same places on faults at regular intervals. The data that REs produce look identical from earthquake to earthquake, and we can use this high similarity in the data to identify REs. Most REs occur on parts of faults that are 'creeping', i.e. the rocks on either side of the fault slide slowly past each other, and do not cause large and damaging earthquakes. By knowing which parts of faults have REs and are therefore creeping, we can better forecast which parts of faults are more and less likely to have damaging earthquakes.

We focus our study on the northern San Francisco Bay Area, where large earthquakes could potentially affect a large regional population. Using a new detection strategy, we find REs on three major faults (the Maacama, Rodgers Creek and Bartlett Springs faults), allowing us to map out where these faults are creeping, and how fast. This information should lead to more accurate future earthquake forecasts.

1 Introduction

The northern San Francisco Bay Area (hereafter 'North Bay') is a region bisected by multiple major strike-slip faults of the Pacific-North America plate boundary in northern California. Between them, the San Andreas, Maacama-Rodgers Creek and Bartlett-Springs-Green Valley fault zones accommodate 38–43 mm/yr of plate boundary-parallel motion [*d'Alessio et al.*, 2005; *Murray et al.*, 2014, Figure 1]. All three major fault zones are considered capable of sustaining damaging ($M \geq 7$) earthquakes that could imperil the local populace; no such event has occurred in over 250 years [*Madden et al.*, 2013; *Field et al.*, 2014]. Such events could potentially affect the greater San Francisco Bay Region (population ~ 7 million), compelling the need to understand the seismic hazard associated with these faults in greater detail.

The seismic hazards posed by several of these structures are complicated by the presence of aseismic fault creep at shallow depths (i.e. $\leq$ 15 km depth). Creep – slow movements of the fault, either continuous or episodic, in the absence of major earthquakes – is a behavior that reduces the rate of moment accumulation on a fault, compared to the case where it is fully locked [e.g. *Field et al.*, 2014]. Experimental studies attribute creep behavior to velocity-strengthening friction [e.g *Dieterich*, 1978; *Ruina*, 1983], suggesting, in addition, that regions of creep on a fault suppress earthquake nucleation [*Dieterich*, 1992; *Scholz*, 1998], and may impede rupture in certain conditions [e.g. *Aagaard et al.*, 2010; *Lozos*, 2013; *Lozos et al.*, 2015]. In order, then, to produce accurate seismic hazard assessments for such faults, we first need a more accurate picture of their creep behavior.

Surface and geodetic observations have been used to infer shallow creep on the Rodgers Creek [at rates of 2-7 mm/yr; *Funning et al.*, 2007; *Jin and Funning*, 2017], Maacama [1–

5 mm/yr; *Harsh et al.*, 1978; *McFarland et al.*, 2016], Bartlett Springs [1–4 mm/yr; *Murray et al.*, 2014; *McFarland et al.*, 2016] and Green Valley faults [1–4 mm/yr; *McFarland et al.*, 2016]. The abundant aseismic afterslip of the West Napa fault following the 2014 South Napa earthquake [e.g. *Floyd et al.*, 2016] suggests that it may also sustain creep. Our knowledge of the creep distribution on these faults is limited – by the sparse spatial coverage of observations, with only a few places where cultural features are offset [e.g. *Harsh et al.*, 1978], only a handful of locations monitored on each fault using alinement arrays [*McFarland et al.*, 2016], dense vegetation limiting InSAR efforts to a short segment of the Rodgers Creek fault [*Funning et al.*, 2007; *Jin and Funning*, 2017], limited continuous GPS coverage and logistical issues with maintaining dense GPS campaign networks, and by the weak resolving power of geodetic observations for slip at depth on strike-slip faults [e.g. *Funning et al.*, 2005; *Page et al.*, 2009].

One means of improving our knowledge of the creep distribution, particularly at depth, comes from repeating earthquakes (REs). REs are sequences of events that produce effectively identical waveforms at common receiving stations. Theoretically, a seismogram waveform can be considered a convolution between the properties of the earthquake source, the response of the receiving station, and the characteristics of the path between them; thus, if two waveforms from different earthquakes at a common station are identical, then the locations and mechanisms of those two earthquakes must also be identical. In addition, many RE sequences have quasi-periodic recurrence [e.g. *Nadeau and Johnson*, 1998; *Igarashi et al.*, 2003], implying that the source is being consistently reloaded to failure. The best current explanation is that REs represent rupture of small fault asperities, surrounded and confined by creep that regularly reloads them to failure [e.g. *Ellsworth and Dietz*, 1990; *Nadeau and Johnson*, 1998; *Schaff et al.*, 1998; *Igarashi et al.*, 2003; *Schaff and Beroza*, 2004; *Chen et al.*, 2007]. In support of this hypothesis, most detected REs to date have been located on faults observed to creep [e.g. *Nadeau et al.*, 1995; *Matsuzawa et al.*, 2002; *Chen et al.*, 2008; *Templeton et al.*, 2008], and simulations support that small asperities surrounded by creep are a viable physical setup for generating REs [*Chen and Lapusta*, 2009; *Richards-Dinger and Dieterich*, 2012].

The implication, then, is that a successful detection of REs on a portion of a fault is consistent with creep at that location. Traditionally, REs have been detected in two ways – by computing pairwise cross-correlation coefficients (CCCs) between individual event waveforms and defining an appropriately high CCC threshold for similarity in the time domain [e.g. *Nadeau et al.*, 1995; *Matsuzawa et al.*, 2002; *Uchida et al.*, 2003; *Igarashi et al.*, 2003; *Chen et al.*, 2008] or frequency domain [e.g. *Templeton et al.*, 2008; *Materna et al.*, 2018], or by estimating precise relative earthquake locations and classifying events as REs if their rupture areas overlap by some percentage [e.g. 50%; *Waldhauser and Ellsworth*, 2000]. Each method has its challenges. CCC thresholding can be subject to false positives (events erroneously identified as repeating), especially when closely spaced events are located far from the detecting station; false negatives (failed detections) can also result in the presence of waveform noise, temporal changes in the crust [e.g. *Poupinet et al.*, 1984; *Schaff et al.*, 2004], or minor differences in rupture propagation. Raising the CCC threshold or frequency bandpass used can reduce false positives, but potentially increase false negatives, and vice-versa, suggesting that RE detection should not solely be based on CCC thresholding alone. In contrast, precise relative event locations require precise relative phase arrival times, but these can be hampered by event origin time errors, lack of nearby well-correlated events, and timing inconsistencies in station clocks [*Rubin*, 2002; *Schaff and Waldhauser*, 2005; *Chen et al.*, 2008].

In this study, we search for REs across the North Bay using a hybrid, multi-stage approach . Our methodology, that we call ‘multi-station clustering’ (described below), allows us to identify a large number of RE families despite a regional seismic network whose configuration changes with time, and incorporates both CCC thresholding and precise relocation.

The result is a detailed, regional-scale view of the creep behavior on the faults of the North Bay for the first time.

2 Data selection and preprocessing

We divide the North Bay study area into 16 subregions, on average 30 × 50 km in dimension, each centered on a fault of interest (Figure S1). We aim for 6000 events or fewer per subregion, and allow for overlap of up to 10 km between subregions to ensure no REs are missed at the edges. We then retrieve event information from the Northern California Earthquake Data Center (NCEDC) for the events within each subregion at nearby stations. We include a station in our event search if it has a duration of operation longer than 10 years, it has detected over 100 events or more in the target subregion, and is located within a zone extending 60 km from the subregion borders. For subregions with good station coverage (e.g. $>$ 150 stations with 100 detected events or more) we raise these thresholds to 15 years and 500 events, respectively. Our final station selections for each subregion range from a minimum of 10 stations to a maximum of 104, with the southernmost subregions typically covered by the greatest numbers of stations.

Considering each subregion in turn and using phase arrival information from the Northern California Seismic Network (NCSN) catalog, we retrieve 20 seconds of vertical component data from the NCEDC archive for each detected event at each station, starting 5 seconds before the P arrival and 15 seconds after. This window size is based on the small sizes (i.e. 'preferred' NCSN catalog magnitude, $M_p < 4$), and therefore short durations of the events, and the short event-station distances (i.e. $<$ 100 km), such that we expect both the P- and S-phase arrivals to occur within it. We band-pass filter each waveform between 1 and 15 Hz, a frequency range that spans most of the energy release of the regional microseismicity [e.g. *Waldhauser and Schaff*, 2008] and resample each station's waveforms to the minimum sample rate for each station's operation time or 100 Hz, whichever is larger.

In total, we retain 674,191 waveforms from $\sim$ 75,000 individual events in the North Bay, spanning the time period 1984–2016. In that interval, the network configuration changed from a minimum of 130 stations to a maximum of 287, with varying spatial coverage and density, with the station distribution particularly sparse in the north (Figures S2 and S3). This varying coverage necessitates a RE detection strategy whereby we identify RE families based upon pairwise similarity of events at different stations at different times, a technique that we call 'multi-station clustering'.

3 Detecting repeating earthquakes using multi-station clustering

We briefly describe below our methodology for selecting and validating RE families from our waveform data set for the North Bay. Further details of each step are provided in supplementary materials. First, considering each station in turn, we calculate CCCs for each pair of events within each applicable subregion, using a 10 second window of data following the catalog P-wave pick time for each event. We employ a new fast frequency domain method, [Super Efficient Cross-Correlation; *Shakibay Senobari et al.*, 2019] that accelerates the calculation by over one order of magnitude compared with other methods. We group together events with high CCCs into clusters, setting a minimum CCC threshold of 0.9 to exclude dissimilar events.

In a key step, we next merge all the clusters for different stations if they share a single event to make multi-station clusters (MSCs) for each subregion. Each event pair in an MSC has a CCC of 0.9 or greater on at least one station. We then make a three-dimensional matrix of CCC values for each MSC. This n × n × m matrix, where n is the number of events in the cluster and m is the number of stations, is populated with the CCCs for each event pair for all detecting stations for a single MSC. A feature of this method is that not every event in a MSC was detected by every station; thus we are able to assemble candidate RE families even when

some of the stations have not operated for the full study duration (Figure 2). Next, we assemble a n × n matrix of averaged CCC values for each MSC from the three-dimensional matrix by taking the average of the six highest CCCs along the station dimension (m). If fewer than six stations (but a minimum of three) detected an individual event pair, we take the average for all those stations. We call the resulting matrix the 'average CCC matrix' for a given MSC. Example of waveforms from such a cluster are shown in Figures 2c and S4.

Next, we apply a nearest-neighbor hierarchical clustering algorithm to each average CCC matrix to identify which of the MSCs are candidate RE families on the basis of their CCCs (Figure 2b). In some cases, MSCs are divided into smaller, sub-clusters on the basis of some connections between events that have lower similarity at common stations (CCC of 0.8 or lower). Ultimately, we retain 120 'candidate RE families'. These contain three or more events, which have high average CCC values for all possible event pair combinations (> 0.9). We also retain 118 single pairs of events with high CCCs ('candidate RE pairs'); all are separated in time by multiple years, unlike some highly correlated event pairs identified in the catalog of *Waldhauser and Schaff* [2008], which are separated by a few days at most.

To validate our candidate RE pairs, we measure precise differential S–P arrival times (Δt_{S-P}), using a cross-spectral method [Figure S5; *Poupinet et al.*, 1984]. We select 1-second windows around the P- and S-phase arrivals for both waveforms in a pair, and cross-correlate them in the frequency domain to obtain Δt_{S-P} at a precision of ~ 0.001 seconds. These relative timing measurements avoid problems with station clock biases. We can compare these values with the theoretical time expected for two earthquake sources with 50% overlap. Assuming circular crack sources [*Eshelby*, 1957] with 3 MPa stress drops, a V_P/V_s ratio of 1.72 and an averaage velocity model [taken from *Klein*, 2014], we would expect $M_p 2$ events (a typical candidate event size) to have $\Delta t_{S-P} \leq 0.008$ seconds; 91 of our RE pair candidates pass this test at all stations (Figures S6 and S7).

For our candidate RE families, we use the HYPODD code [*Waldhauser and Ellsworth*, 2000] and the methodology of *Chen et al.* [2008] to estimate precise relative locations of those events and test their validity as REs. In this procedure, we use only Δt_{S-P} measurements for each pair combination in a family, as described above, with a 1D velocity model provided for this area [*Klein*, 2014]. We relocate the events in each family separately (e.g. Figure 3), so that only the highest CCC combinations are used. The resulting relative locations can then be compared with the expected circular crack dimensions, as described above, to check for source region overlap. Overall, we find that 59 of our candidate RE families pass this relocation test (hereafter, 'confirmed REs'), and that a further 48 families, despite high CCC values, have insufficient data coverage to allow stable relocations ('possible REs'). This is a significantly higher number of RE families than identified in the North Bay by 'conventional' means – *Xu et al.* [2018], using only long-lived stations, find only 4 RE sequences on the Rodgers Creek fault, compared with 36 in this study (15 confirmed, 7 possible, 14 pairs; Figure S8) – showing the importance of using the multi-station clustering approach.

4 How the repeating earthquakes are distributed

The locations of our RE families – confirmed, possible and pairs – are plotted in map view in Figure 1 and as profiles in Figure 4, with their temporal behavior in Figure S9. The majority ($\sim 90\%$) are located along the major inland fault zones – the Rodgers Creek-Maacama and Green Valley-Bartlett Springs faults – with a few located on minor, intermediate structures. This concentration of REs along major faults with observed creep is once again suggestive of a relationship between these two phenomena.

The Maacama fault shows the greatest amount of RE activity of the faults in the region. The along-strike cross-section (profile S1-T1; Figure 4) shows that REs are pervasive along the fault. The maximum depth of REs increases, gradually, from south to north, from $\sim$ 5 km near Cloverdale in the south, to $\sim$ 11 km NW of Willits in the north. The majority

of these RE families and pairs occur within a prominent band, or 'streak' in the relocated seismicity, which also increases in depth along-strike to the northwest. Such streaks of microearthquakes have been identified and associated with creep on other faults [e.g. *Rubin et al.*, 1999].

The pattern of REs at Cloverdale defines two subparallel dipping structures in the 1–7 km depth range, approximately 2–3 km apart (profiles A5-B5 to A7-B7; Figure 4). The eastern of the two structures aligns with the mapped Holocene Maacama fault trace at the surface; it is not clear if the western structure has surface expression, although there are Quaternary structures mapped in the vicinity [*U.S. Geological Survey and California Geological Survey*, 2007]. To our knowledge, this is the first evidence suggesting two currently active fault segments in this area, and that both may be creeping at shallow depths.

At Willits, the deepest REs are aligned with the NE-dipping trend of microearthquakes that have previously been attributed to the $\sim 60°$-dipping main surface of the Maacama fault [e.g. *Waldhauser and Ellsworth*, 2000, profiles A1–B1 to A3–B3; Figure 4], suggesting that this structure could be creeping in the depth range 7–10 km. More intriguingly, the shallower REs in the area, located at depths of 1–5 km, define a subvertical trend that projects to the surface $\sim$ 5 km NE of the main Maacama surface trace, suggesting that there is a subvertical shallow splay fault at this location that may also be creeping (profile A3–B3; Figure 4). This putative shallow subvertical splay at Willits projects to the location of a prominent Quaternary fault scarp on the east side of Little Lake Valley. This structure is variously referred to as the 'East Willits fault' [*Prentice et al.*, 2014] or the 'East Valley fault' [*Woolace*, 2005], and was recognized in the 1970s [*Simon et al.*, 1978]. Our results indicate, for the first time, to our knowledge, that this fault may be actively creeping.

On the Rodgers Creek fault the majority of REs are clustered along a section extending $\sim$ 30 km northwestwards from the city of Santa Rosa. Shallow creep (up to $\sim$ 2 km depth) is inferred along this segment from InSAR data [*Funning et al.*, 2007; *Jin and Funning*, 2017], further confirming the association of REs with creep. In cross-section, these REs define a plane that dips steeply to the northeast, at depths of 1.4–7.0 km (Figure 4), extending our knowledge of the creeping zone to those depths.

We identify REs across a wide range of depths (1–15 km) on the central Bartlett Springs fault, in a zone extending around 20 km NW of Lake Pillsbury (profiles S2–T2 and A4–B4; Figure 4). This is a location where both alinement array data and GPS data are consistent with surface creep at around 3–4 mm/yr [*Murray et al.*, 2014; *McFarland et al.*, 2016]. The distribution of REs implies that creep could be occurring across the full seismogenic depth of the fault along this zone. Elsewhere along the fault, the RE families and pairs are more diffuse, making it difficult to make definite statements on the likely distribution of creep.

Finally, we identify two RE groups – a periodic RE family and a RE pair – on the West Napa fault. The former, composed of three repeating events (in 1995, 2000 and 2005) is located on the Browns Valley segment of the fault, $\sim$ 4 km NW of the northern end of the 2014 earthquake rupture zone [e.g. *Floyd et al.*, 2016] and at 6 km depth. The 2014 M6.0 South Napa earthquake showed abundant shallow aseismic afterslip, including slip on the southern portion of the Browns Valley segment, however no previous studies had identified any interseismic creep on the West Napa fault [e.g. *Funning et al.*, 2007]. The identification of repeating events on the West Napa fault suggests that portions of it may have been creeping prior to the 2014 event, albeit at a rate and depth that may not be detectable at the surface using geodetic data.

5 Estimating creep rates from creeping event recurrences and magnitudes

Based on the time- and slip-predictable behavior of REs on the San Andreas fault at Parkfield, *Nadeau and Johnson* [1998] proposed that RE moment, M_0 (in dyne-cm), could be

converted to fault slip, d_i (in cm), by the relation,

$$d_i = 10^{\alpha} M_0^{\beta} \tag{1}$$

where $\alpha = -2.36 \pm 0.16$ and $\beta = 0.17 \pm 0.01$ are empirical constants chosen to relate the RE moment release and recurrence to average creep rate based on the geodetic model of *Harris and Segall* [1987]. By dividing these estimates by the mean RE recurrence interval, we can estimate the creep rate in the vicinity of a RE family.

This calibration has been used in several studies and provided meaningful results in other settings [e.g. *Chen et al.*, 2007; *Uchida and Matsuzawa*, 2013; *Yu*, 2013]. However, when we apply it to our RE families, using the sequences with the most robustly estimated recurrence intervals (those with coefficients of variation of 0.4 or better), we obtain creep rates that are $\sim$ 3 times higher than those derived geodetically – e.g. $\sim 7 - 13$ mm/yr from REs compared with $\sim 2 - 4$ mm/yr from InSAR on the northern Rodgers Creek fault [*Jin and Funning*, 2017; *McFarland et al.*, 2016, Figures S10 and S11].

Such large overestimates suggest that the calibration of *Nadeau and Johnson* [1998] may not be applicable to the faults of the North Bay, perhaps due to a difference in fault lithology and rheology, or the significantly slower fault slip rates in the region [e.g. *Parsons et al.*, 2013]. *Chen et al.* [2007] suggested that the slope of RE moment versus recurrence interval could be universal but the intercept can be a function of slip rate, recalibrating this intercept for each region based on its slip rates. We adopt the same philosophy, recalibrating the moment–slip relationship (Equation 1) and obtain a revised value of $\alpha = -2.86$ using a shallow RE family from the Rodgers Creek fault [1.4 km depth; *Waldhauser and Schaff*, 2008] and the shallow creep rate estimated there from InSAR [2.7 mm/yr; *Jin and Funning*, 2017].

The distribution of RE creep rates under this revised calibration is plotted in Figures 1 and 4. We obtain creep rates of 1–6 mm/yr on the Maacama fault, 1–4 mm/yr on the Rodgers Creek fault, and 2–6 mm/yr on the Bartlett Springs fault. The structurally complex southern Maacama fault creeps at 3 mm/yr or less; in the north near Willits, estimated creep rates are higher (5–6 mm/yr) on REs vertically below the surface trace of the East Willits fault. This may explain the discrepancy between the $\sim$ 10 mm/yr creep rates here in the GPS-based model of *Murray et al.* [2014] and the 5–6 mm/yr surface creep rate on the main Maacama trace obtained by *McFarland et al.* [2016] – the additional slip rate detected by GPS could plausibly be on the East Willits structure. Creep on the Rodgers Creek fault is consistent within error of the surface rates obtained by InSAR [*Jin and Funning*, 2017], and is self-consistent between RE sequences (Figures S10–S12). The highest creep rates (5–6 mm/yr) on the Bartlett Springs fault are at the base of the upper crust (11–15 km), again in keeping with the GPS data and modeling of *Murray et al.* [2014], who infer faster creep below 5 km than at the surface; slower rates (3–4 mm/yr) at shallower depths, are also consistent with the GPS data. Intriguingly, we obtain very similar creep rates using an alternative calibration [$\alpha = -1.56, \beta = 0.10$; *Khoshmanesh et al.*, 2015, Figures S10 and S11], suggesting that the parameters α and β may trade off against each other, a situation that warrants further investigation in future.

6 Discussion and conclusions

Searching for REs on the faults of the North Bay reveals results consistent with widespread creep behavior. Only a handful of the REs we identify would be found by CCC thresholding without making use of a multi-station clustering approach, given the sparse and changing configuration of the seismic network in the region. The Maacama fault, in particular, shows creep along most of its length, with REs consistently found within a streak of seismicity that deepens to the north. The southern Maacama fault near Cloverdale and its northern portion near Willits both show evidence for structural complexity, with two possibly creeping subparallel fault strands highlighted by REs. Elsewhere, the northern Rodgers Creek fault likely

creeps down to 7 km depth along a segment identified as creeping by InSAR, and the central Bartlett Springs fault has a distribution of REs consistent with creep across its full seismogenic width. These results, in concert with geological mapping, may provide additional constraints on the lithological conditions that support creep.

We suggest that a new, region-specific calibration of the magnitude-recurrence 'creepmeter' is required to obtain plausible creep rates from these North Bay REs, implying that the Parkfield calibration of *Nadeau and Johnson* [1998] may not be universally applicable. The creep rates we obtain via this analysis broadly agree with those obtained by geodetic studies of the Rodgers Creek and Bartlett Springs faults [*Murray et al.*, 2014; *Jin and Funning*, 2017], and can resolve a discrepancy between observed and modeled creep rates on the northern Maacama fault [e.g. *Murray et al.*, 2014; *McFarland et al.*, 2016] by identifying a second creeping structure that may accommodate additional slip.

Widespread creep on the North Bay faults would impact their potential seismic hazard by reducing both their strain accumulation rates and the area of each fault able to sustain full seismic rupture. Dynamic rupture simulations show that the viability of a partially-creeping fault segment for throughgoing fault rupture depends to some extent on the relative down-dip widths of locked and creeping zones on a fault [*Lozos*, 2013; *Lozos et al.*, 2015]. While such analysis is beyond the scope of this study, our results may provide useful subsurface constraints on such scenario models in future.

Acknowledgments
This study was supported by USGS award G16AP00034. N.S.S. acknowledges additional support from NASA NESSF award NNX15AM66H. We thank David Guenaga for assistance with data retrieval, Bob Nadeau for helpful suggestions at the start of the project, and Michael Yeh, Eamonn Keogh and Yan Zhu for useful discussions about similarity search and clustering. Kate Chen and Amanda Thomas provided constructive reviews that have helped to improve the manuscript – thank you to both. Some of the figures were produced using the Generic Mapping Tools [*Wessel et al.*, 2013], and using color maps produced by *Kovesi* [2015].

References

Aagaard, B. T., R. W. Graves, D. P. Schwartz, J. J. Lienkaemper, D. A. Ponce, and R. Graymer (2010), Ground motion modeling of Haward fault scenario earthquakes I: Construction of the suite of scenarios, *Bull. Seismol. Soc. Am.*, doi:100(6), 2927-2944.

Chen, K. H., R. M. Nadeau, and R.-J. Rau (2007), Towards a universal rule on the recurrence interval scaling of repeating earthquakes?, *Geophys. Res. Lett.*, *34*, L16308, doi: 10.1029/2007GL030554.

Chen, K. H., R. M. Nadeau, and R.-J. Rau (2008), Characteristic repeating microearthquakes on an arc-continent collision boundary – the Chihshang fault of eastern Taiwan, *Earth Planet. Sci. Lett.*, *276*, 262–272, doi:10.1016/j.epsl.2008.09.021.

Chen, T., and N. Lapusta (2009), Scaling of small repeating earthquakes explained by interaction of seismic and aseismic slip in a rate and state fault model, *J. Geophys. Res.*, *114*, B01311, doi:10.1029/2008JB005749.

d'Alessio, M. A., I. A. Johanson, R. Bürgmann, D. A. Schmidt, and M. H. Murray (2005), Slicing up the San Francisco Bay Area: Block kinematics and fault slip rates from GPS-derived surface velocities, *J. Geophys. Res.*, *110*, B06403, doi:doi:10.102/2004JB003496.

Dieterich, J. H. (1978), Time-dependent friction and the mechanics of stick-slip, *Pure. Appl. Geophys.*, *116*, 790–806.

Dieterich, J. H. (1992), Earthquake nucleation on faults with rate-and state-dependent strength, *Tectonophys.*, *211*, 115–134, doi:10.1016/0040-1951(92)90055-B.

Ellsworth, W. L., and L. D. Dietz (1990), Repeating earthquakes: characteristics and implications, *Tech. rep.*, U.S. Geol. Surv., Menlo Park, Calif.

Eshelby, J. D. (1957), The determination of the elastic field of an ellipsoidal inclusion and related problems, *Phil. Trans. R. Soc. Lond. A*, *241*, 376–396.

Field, E. H., R. J. Arrowsmith, G. P. Biasi, P. Bird, T. E. Dawson, K. R. Felzer, D. D. Jackson, K. M. Johnson, T. H. Jordan, C. Madden, A. J. Michael, K. R. Milner, M. T. Page, T. Parsons, P. M. Powers, B. E. Shaw, W. R. Thatcher, R. J. Weldon, and Y. Zeng (2014), Uniform California Earthquake Rupture Forecast, version 3 (UCERF3) – the time-independent model, *Bull. Seismol. Soc. Am.*, *104*, 1122–1180, doi:10.1785/0120130164.

Floyd, M. A., R. J. Walters, J. R. Elliott, G. J. Funning, J. L. Svarc, J. R. Murray, A. J. Hooper, Y. Larsen, P. Marinkovich, R. Bürgmann, I. A. Johnason, and T. J. Wright (2016), Spatial variations in fault friction related to lithology from rupture and afterslip of the 2014 South Napa, California, earthquake, *Geophys. Res. Lett.*, *43*, 6808–6816, doi:10.1002/2016GL069428.

Funning, G. J., B. Parsons, T. J. Wright, J. A. Jackson, and E. J. Fielding (2005), Surface displacements and source parameters of the 2003 Bam (Iran) earthquake from Envisat advanced synthetic aperture radar imagery, *J. Geophys. Res.*, *110*, B09406.

Funning, G. J., R. Bürgmann, A. Ferretti, F. Novali, and A. Fumagalli (2007), Creep on the Rodgers Creek fault, northern San Francisco Bay area, from a 10-year PS-InSAR dataset, *Geophys. Res. Lett.*, *34*, L19306, doi:10.1029/2007GL030836.

Harris, R. A., and P. Segall (1987), Detection of a locked zone at depth on the Parkfield, California, segment of the San Andreas fault, *J. Geophys. Res.*, *92*, 7945–7962.

Harsh, P. W., E. H. Pampeyan, and J. M. Coakley (1978), Slip on the Willits fault, California, *Earthquake Notes*, *49*, 22.

Igarashi, T., T. Matsuzawa, and A. Hasegawa (2003), Repeating earthquakes and interplate aseismic slip in the northeastern Japan subduction zone, *J. Geophys. Res.*, *86*(2249), doi:10.1029/2002JB001920.

Jin, L., and G. J. Funning (2017), Testing the inference of creep on the northern Rodgers Creek fault, California, using ascending and descending persistent scatterer InSAR data, *J. Geophys. Res.*, *122*, 2373–2389, doi:10.1002/2016JB013535.

Khoshmanesh, M., M. Shirzaei, and R. M. Nadeau (2015), Time-dependent model of aseismic slip on the central San Andreas fault from InSAR time series and repeating earthquakes, *J. Geophys. Res.*, *120*, 6658–6679.

Klein, F. (2014), Hypoinverse, v 1.40, ftp://ehzftp.wr.usgs.gov/klein/hyp1.40, Last accessed 2019/03/07.

Kovesi, P. (2015), Good Colour Maps: How to Design Them, *arXiv e-prints*, arXiv:1509.03700.

Lozos, J. C. (2013), Dynamic rupture and ground motion modeling on realistically complex strike-slip faults, Phd dissertation, University of California, Riverside.

Lozos, J. C., R. A. Harris, J. R. Murray, and J. J. Lienkaemper (2015), Dynamic rupture models of earthquakes on the Bartlett Springs Fault, Northern California, *Geophys. Res. Lett.*, *42*, 4343–4349, doi:10.1002/2015GL063802.

Madden, C., D. E. Haddad, S. J. B, O. Zielke, J. R. Arrowsmith, R. Weldon, and J. Colunga (2013), Appendix R–Compilation of slip-in-the-last-event data and analysis of last event, repeated slip, and average displacement for recent and prehistoric ruptures, in *The Uniform California Earthquake Rupture Forecast, version 3 (UCERF 3)*, p. 65 pp., U.S. Geol. Surv. Open-File Rept. 2013-1165-D, and California Geol. Surv. Special Rept. 228-D.

Materna, K., T. Taira, and R. Bürgmann (2018), Aseismic transform fault slip at the Mendocino Triple Junction from characteristically repeating earthquakes, *Geophys. Res. Lett.*, *45*, 699–707, doi:10.1002/2017GL075899.

Matsuzawa, T., T. Igarashi, and A. Hasegawa (2002), Characteristic small-earthquake sequence off Sanriku, northeastern Honshu, Japan, *Geophys. Res. Lett.*, *29*, 1801, doi:10.1029/2001GL014632.

McFarland, F. S., J. J. Lienkaemper, and S. J. Caskey (2016), Data from theodolite measurements of creep rates on San Francisco Bay region faults, California, *Open File Rep. 2009-1119 v1.8*, U.S. Geol. Surv., Menlo Park, Calif.

Murray, J. R., S. E. Minson, and J. L. Svarc (2014), Slip rates and spatially variable creep on faults of the northern San Andreas system inferred through Bayesian inversion of Global Positioning System data, *J. Geophys. Res.*, *119*, 6023–6047, doi:10.1002/2014JB010966.

Nadeau, R. M., and L. R. Johnson (1998), Seismological studies at Parkfield VI: Moment release rates and estimates of source parameters for small repeating earthquakes, *Bull. Seismol. Soc. Am.*, *267*, 790–804.

Nadeau, R. M., W. Foxall, and T. V. McEvilly (1995), Clustering and periodic recurrence of microearthquakes on the San Andreas Fault at Parkfield, California, *Science*, *267*, 503–507.

Page, M. T., S. Custódio, R. J. Archuleta, and J. M. Carlson (2009), Constraining earthquake source inversions with GPS data: 1. resolution-based removal of artifacts, *J. Geophys. Res.*, *114*, B01314, doi:10.1029/2007JB005449.

Parsons, T., K. M. Johnson, P. Bird, J. Bormann, T. E. Dawson, E. H. Field, W. C. Hammond, T. A. Herring, R. McCaffrey, Z.-K. Shen, W. R.Thatcher, R. J. Weldon, and Y. Zeng (2013), Appendix C – Deformation models for UCERF3, in *Uniform California Earthquake Rupture Forecast, Version 3 (UCERF3) – The Time-Independent Model*, edited by Working Group on California Earthquake Probabilities, U.S. Geological Survey Open-File Report 2013-1165, Menlo Park, CA.

Poupinet, G., W. L. Ellsworth, and J. Frechet (1984), Monitoring velocity variations in the crust using earthquake doublets: an application to the Calaveras fault, California, *J. Geophys. Res.*, *89*, 5719–5731.

Prentice, C. S., M. C. Larsen, H. M. Kelsey, and J. Zachariasen (2014), Late Holocene slip rate and ages of prehistoric earthquakes along the Maacama fault near Willits, Mendocino County, northern California, *Bull. Seismol. Soc. Am.*, *104*, 2966–2984, doi: 10.1785/0120140003.

Richards-Dinger, K., and J. H. Dieterich (2012), RSQSim earthquake simulator, *Seismol. Res. Lett.*, *83*, 983–990, doi:10.1785/0220120105.

Rubin, A. M. (2002), Using repeating earthquakes to correct high-precision earthquake catalogs for time-dependent station delays, *Bull. Seismol. Soc. Am.*, *92*, 1647–1659.

Rubin, A. M., D. Gillard, and J.-L. Got (1999), Streaks of microearthquakes along creeping faults, *Nature*, *400*, 635–641.

Ruina, A. (1983), Slip instability and state variable friction laws, *J. Geophys. Res.*, *88*, 10,359–10,370.

Schaff, D. P., and G. C. Beroza (2004), Coseismic and postseismic velocity changes measured by repeating earthquakes, *J. Geophys. Res.*, *109*, B10302, doi: 10.1029/2004JB003011.

Schaff, D. P., and F. Waldhauser (2005), Waveform cross-correlation based differential travel-time measurements at the Northern California Seismic Network, *Bull. Seismol. Soc. Am.*, *95*, 2446–2461, doi:10.1785/012004022.

Schaff, D. P., G. C. Beroza, and B. E. Shaw (1998), Postseismic response of repeating aftershocks, *Geophys. Res. Lett.*, *25*, 4549–4552.

Schaff, D. P., G. H. R. Bokelmann, W. L. Ellsworth, E. Zanzerkia, F. Waldhauser, and G. C. Beroza (2004), Optimizing correlation techniques for improved earthquake location, *Bull. Seismol. Soc. Am.*, *94*, 705–721.

Scholz, C. (1998), Earthquakes and friction laws, *Nature*, *391*, 37–42, doi:10.1038/34097.

Shakibay Senobari, N., G. J. Funning, E. Keogh, Y. Zhu, C. M. Yeh, Z. Zimmerman, and A. Mueen (2019), Super-Efficient Cross-Correlation (SEC-C): A fast matched filtering code suitable for desktop computers, *Seismol. Res. Lett.*, *90*, 322–334, doi: 10.1785/0220180122.

Simon, R. B., E. H. Pampeyan, and C. W. Stover (1978), The Willits, California, magnitude-4.8 earthquake of November 22, 1977, *Open File Rep. 78-1075*, U.S. Geol. Surv., Menlo

Park, Calif.

Templeton, D. C., R. M. Nadeau, and R. Bürgmann (2008), Behavior of repeating earthquake sequences in central California and the implications for subsurface fault creep, *Bull. Seismol. Soc. Am.*, *98*, 52–65, doi:10.1785/0120070026.

Uchida, N., and T. Matsuzawa (2013), Pre- and postseismic slow slip surrounding the 2011 Tohoku-oki earthquake rupture, *Earth Planet. Sci. Lett.*, *374*, 81–91, doi:10.1016/j.epsl.2013.05.021.

Uchida, N., T. Matsuzawa, A. Hasegawa, and T. Igarashi (2003), Interplate quasi-static slip off Sanriku, NE Japan, estimated from repeating earthquakes, *Geophys. Res. Lett.*, *30*, 1801, doi:10.1029/2003GL017452.

U.S. Geological Survey, and California Geological Survey (2007), Quaternary fault and fold database for the United States, http//earthquake.usgs.gov/regional/qfaults/.

Waldhauser, F. (2009), Near-real-time double-difference event location using long-term seismic archives, with application to Northern California, *Bull. Seismol. Soc. Am.*, *99*, 2736–2748, doi:10.1785/0120080294.

Waldhauser, F., and W. L. Ellsworth (2000), A double-difference earthquake location algorithm: Method and application to the northern Hayward fault, *Bull. Seismol. Soc. Am.*, *90*, 1353–1368.

Waldhauser, F., and D. P. Schaff (2008), Large-scale relocation of two decades of Northern California seismicity using cross-correlation and double-difference methods, *J. Geophys. Res.*, *113*, B08331, doi:10.1029/2007JB005479.

Wessel, P., W. H. F. Smith, R. Scharroo, J. F. Luis, and F. Wobbe (2013), Generic mapping tools: Improved version released, *Eos Trans. AGU*, *94*, 409–410, doi:10.1002/2013EO450001.

Woolace, A. C. (2005), Late Neogene and Quaternary stratigraphy and structure of Little Lake Valley, northern Coast Range, California, M.S. thesis, Humboldt State University, Arcata, CA.

Xu, W., S. Wu, K. Materna, R. Nadeau, M. Floyd, G. Funning, E. Chaussard, C. W. Johnson, J. R. Murray, X. Ding, and R. Bürgmann (2018), Interseismic ground deformation and fault slip rates in the greater San Francisco Bay Area from two decades of space geodetic data, *J. Geophys. Res.*, *123*, 8095–8109, doi:10.1029/2018JB016004.

Yu, W. (2013), Shallow-focus repeating earthquakes in the Tonga-Kermadec-Vanuatu subduction zones, *Bull. Seismol. Soc. Am.*, *103*(1), 463–486, doi:10.1785/0120120123.

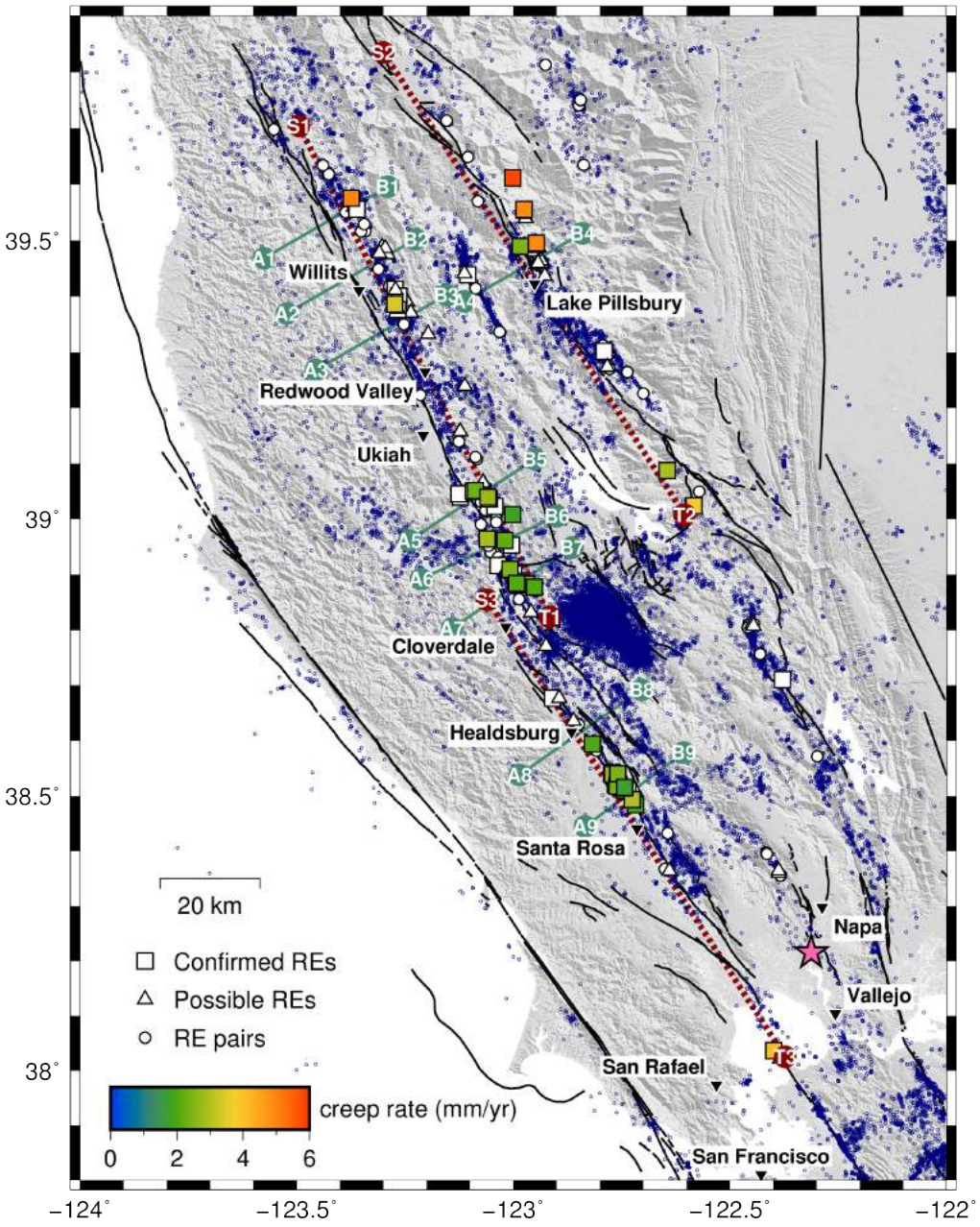

Figure 1. Faults, seismicity and repeating earthquake (RE) locations in the northern San Francisco Bay Area. Major faults are indicated by solid black lines. The majority of confirmed RE families (validated by precise relocation; squares), possible RE families (cross-correlation coefficients >0.9; triangles) and RE pairs (validated by Δt_{S-P}; circles) are focused along the Rodgers Creek, Maacama and Bartlett Springs faults, indicating that these faults are likely to be creeping along much of their lengths. Further details are given in the main text. Color-coding of the RE symbols indicates the estimated creep rate at that location. Locations of cross-fault (A–B; sea green) and along-strike (S–T; dark red) profiles corresponding to Figure 4 are marked. Relocated seismicity from the near-real time double difference catalog for northern California [*Waldhauser*, 2009] is plotted as dark blue dots; epicenter of the 2014 South Napa earthquake is plotted as a pink star.

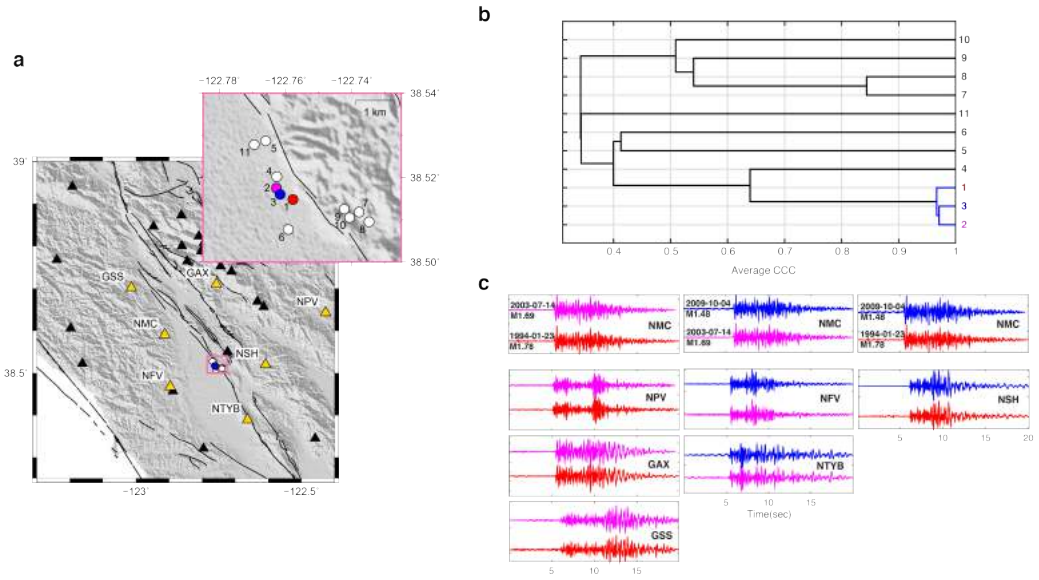

Figure 2. Hierarchical and multi-station clustering. (a) Map of seismic stations in the vicinity of the Rodgers Creek fault (triangles; named stations in gold). Pink box shows the catalog locations of 11 numbered earthquakes (circles). (b) Hierarchical clustering of average cross-correlation coefficients (CCCs) for the 11 earthquakes. Groups of similar events (e.g. 1, 2 and 3; 7 and 8) have high average CCCs, and tend to be located close together. Connections between groups or individual events are made between the most similar members of those groups (the 'nearest neighbors' in terms of similarity). For example, the highest average CCC between event 4 and the members of the event 1, 2, 3 group, is 0.64 between events 3 and 4, and we use that value to represent the degree of similarity between event 4 and the group. (c) Example of a multi-station cluster. Events 1, 2 and 3 (waveforms in red, magenta and blue) can be assembled into a cluster based upon their pairwise waveform similarity at multiple different stations, even though only one station, NMC, detected all three.

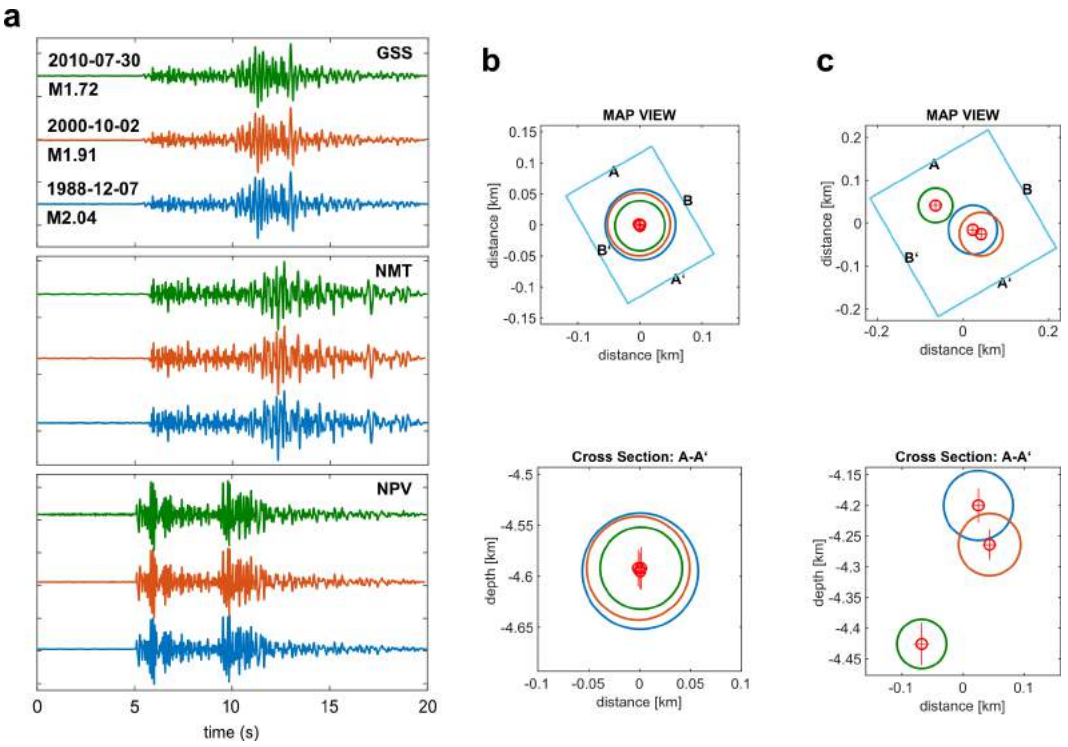

Figure 3. Validation of repeating earthquake (RE) locations using precise relocation. (a) Example waveforms at three stations from a three event RE sequence on the Rodgers Creek fault near Santa Rosa (1998/12/07, blue; 2000/10/02, orange; 2010/07/30, green). (b) Precise relocations from this study, using differential S–P times between pairs of events in a sequence, from stations where high cross-correlation coefficients were estimated. Distribution of hypocenters (small red circles, with uncertainties indicated by red crosses), and source areas (large circles, color-coded by event) are shown in both map view (top) and fault-parallel cross-section view (bottom). The source areas for the three events overlap almost completely, suggesting that these are indeed REs. (c) Similar to (b) except locations for the three events are taken from the double-difference relocated catalog of *Waldhauser and Schaff* [2008]. Location biases, perhaps caused by station or origin timing errors that can be present in the absolute P- and S-wave arrival times used in the catalog, mean that these events would not be selected as REs from their catalog locations, which do not permit sufficient overlap in source areas. Our precise relocations, based only on differential travel times, are not susceptible to such biases.

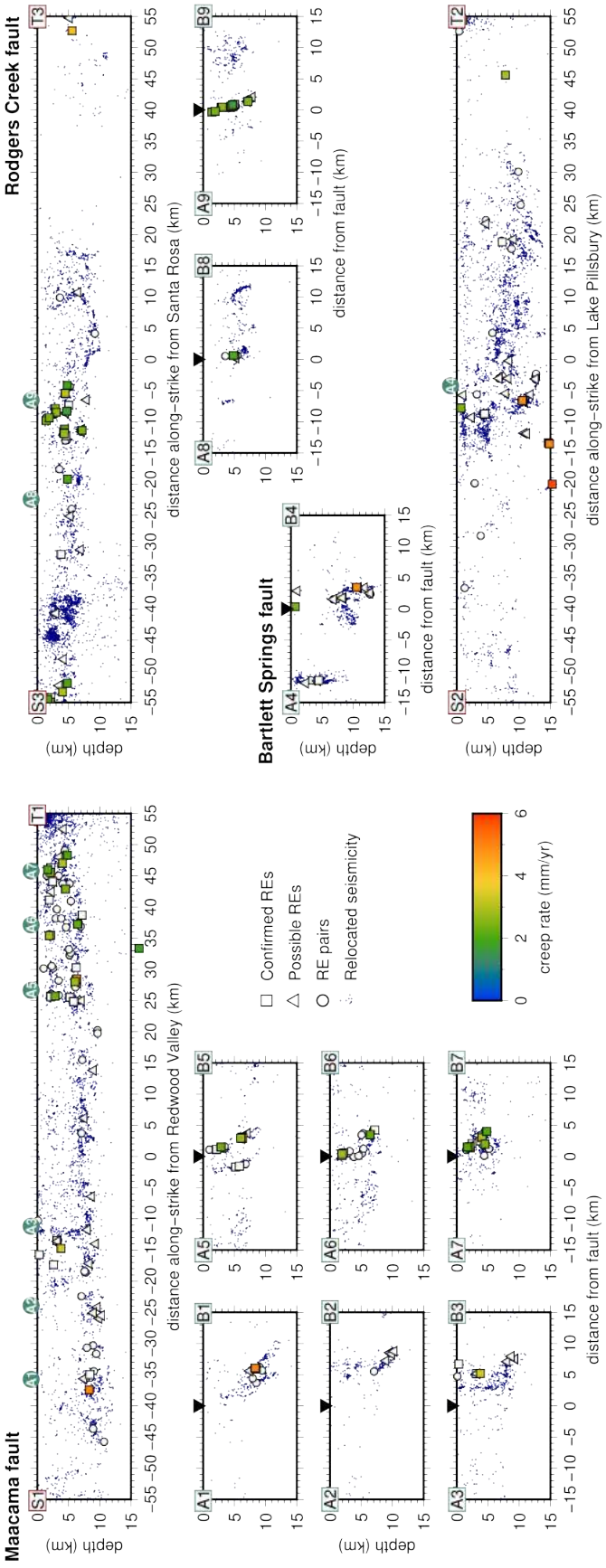

Figure 4. Along-strike and strike-perpendicular cross-sections through our repeating earthquake (RE) locations. RE categories, symbols and profile locations are shown in Figure 1. The Maacama fault (profile S1–T1) shows a band of REs along its full length that tracks a streak in the microseismicity. In detail, the pattern of REs is complex, defning a vertical splay off of the dipping microseismic trend of the main fault strand near Willits (A1–B1 to A3–B3), and subparallel dipping structures in the southeast near Cloverdale (A5–B5 to A7–B7). The Bartlett Springs fault (S2–T2) has a concentration of REs near Lake Pillsbury, spanning its full seismogenic width (A4–B4). On the Rodgers Creek fault (S3–T3), REs are focused along a short segment 5–20 km NW of Santa Rosa, defining a steep-dipping plane to ~ 7 km (A8–B8 and A9–B9). [Positive distances are to the SE.]

Supporting Information for

"Widespread fault creep in the northern San Francisco Bay Area revealed by multi-station cluster detection of repeating earthquakes"

Nader Shakibay Senobari[1,2], **Gareth J. Funning**[1]

[1]Department of Earth and Planetary Sciences, University of California, Riverside, CA

[2]Now at Department of Computer Science and Engineering, University of California, Riverside, CA

Contents

1. Text S1
2. Figures S1 to S12

Additional Supporting Information (Files uploaded separately)

1. Data Set S1: Catalog of confirmed repeating earthquakes
2. Data Set S2: Catalog of possible repeating earthquakes
3. Data Set S3: Catalog of repeating earthquake pairs
4. Data Set S4: Estimated creep rates from confirmed repeating earthquakes
5. Data Set S5: Estimated creep rates from possible repeating earthquakes

Corresponding author: Nader Shakibay Senobari, nshak006@ucr.edu

Text S1. Detecting repeating earthquakes using multi-station clustering

1.1 Single station clusters

For each station in turn we start by calculating the normalized cross-correlation coefficient (CCC) for each pair of earthquake within each associated subregion, and grouping similar events together. We use the Super Efficient Cross-Correlation algorithm [SEC-C; *Shakibay Senobari et al.*, 2019] to compute these values. By concatenating all of the event waveforms that are to be compared to a template waveform together, SEC-C can calculate thousands of CCCs simultaneously in the frequency domain, accelerating the calculation by over one order of magnitude compared with other methods for pairwise similarity search. We take care with this concatenation and template waveform selection to minimize the number of redundant calculations (i.e. to avoid unnecessary repeat comparisons). Next, we group together events with high CCCs at each given station into 'single station clusters', setting a minimum CCC threshold of 0.9. Note that at this stage this threshold is designed to exclude dissimilar events, rather than definitively select repeating events. Note also that we retain CCC values for pairs of events that are not included in these single-station clusters.

1.2 Multi-station clusters

We next merge all the single station clusters for different stations that share a common event to make 'multi-station clusters' (MSCs) in each subregion. Each event pair in a MSC has a CCC of 0.9 or greater on at least one station. We then make a three-dimensional matrix of CCC values for each MSC. This $n \times n \times m$ matrix, where n is the number of events in the cluster and m is the number of stations, is populated with the CCCs for each event pair for all detecting stations for a single MSC. Note that (i) not every event pair has a high CCC value at every station, and (ii) not every event in a MSC was detected by every station – in those cases, the corresponding elements of the matrix are assigned a null value.

In the next step, we make a $n \times n$ matrix of averaged CCC values for each event pair from the $n \times n \times m$ matrix for each MSC by taking the average for the six highest CCCs along the station dimension (m). If fewer than six stations detected an individual event pair, we take the average for all available detecting stations, so long as there are at least three. If less than three stations (two or less) exist for an event pair, we assign a null value to that pair. We call the resulting matrix the 'average CCC matrix' for a given MSC. Therefore, each CCC value in this matrix not only represents the similarity between event pairs at multi-stations, but also

indicates that at least three stations detected this pair. Example of waveforms from such a cluster are shown in Figure 2 in the main text.

1.3 Hierarchical clustering

Taking the average CCC matrices for each MSC, we next employ an RE selection method that makes use of hierarchical clustering of the average CCC values for each event pair (Figure S4). An advantage of using a hierarchical clustering approach is that we can visualize the multi-station similarity of an RE family with itself and with nearby seismicity.

We use the hierarchical clustering algorithm *linkage* and the plotting routine *dendrogram* within MATLAB to produce dendrograms – tree diagrams showing the hierarchy of similarity between events in a cluster based on average CCC values. *linkage* by default uses a nearest-neighbor criterion to assess how 'close' individual events or groups of events are to each other. We use Euclidean distance (1−average CCC) as a proxy for the 'distances' between events, thus highly correlated events with high average CCCs are considered close to each other. The combination of both multi-station and hierarchical clustering using this nearest neighbor approach is our solution to the problem of temporal changes to the network. The lack of long-lived stations that recorded all events in a RE family is particularly problematic when the recurrence interval is large.

For example if we have three members – A, B and C – of an RE family and if we assume they recurred every $\sim$ 12 years, the probability of having several nearby stations (e.g. within 60 km of the epicenters) operating for at least 24 years without instrument changes is low. Using the approach described here, this RE family can be detected if, for example, both A and B are recorded at three or more common stations, and then both B and C are recorded at three or more different common stations. In this case, using hierarchical clustering with the nearest neighbor approach, event C becomes connected to the pair A and B as it is connected to B in the average CCC matrix. To connect another possible member of this family (event D), it should have high CCCs at three or more stations with at least one of the other members (i.e. A, B or C). In other words, our approach systematically detects families if the members of that family have two characteristics: (i) Each member of the family should have high CCCs (e.g. average 0.95) at three or more stations with at least one other member, and (ii) there should be sufficient links between pairs of events in a family such that a path exists

from any member to any other member. In the example above, the path from A to C is via event B as there is no direct path from A to C.

We plot the dendrograms for each average CCC matrix, using a graphical user interface (GUI) that also provides magnitude and event time information for each event cluster. Using this GUI at the same time we check the CCC values between sequences, magnitudes of events within clusters, origin times and also the CCC values at nearby stations. Note that although we chose 0.9 for the CCC threshold for single station clustering, for the average CCC matrices the minimum average CCC values can be as low as 0.7. Empirically, we observe that more distant stations have less sensitivity to differences between events than stations located closer by; thus, if the station reporting the highest CCC is the most distant, the average CCC value can be much lower than the maximum value.

We retain these low CCC connections to assess the similarity of RE sequences with each other and also nearby events. In those cases where each cluster contains many events and/or subclusters making visual inspection impractical, we break such 'major' clusters into smaller, 'minor' clusters by disconnecting the linkage between them. We achieve this by applying a high CC threshold (e.g. 0.85, 0.9 or 0.95, based on the size of the main cluster). The lowest CCC threshold we accept for such visual inspection is 0.8. In most cases, using a CCC threshold of 0.8, RE family candidates become disconnected from nearby events (e.g. Figure S4).

1.4 Measuring precise differential S–P times

In order to confirm that REs come from the same source region on a fault or not (i.e. to check if our high CCC clusters are false positive detections), we apply a check on event similarity based on similarity of location. We consider a pair of events to be REs if their source regions overlap by at least 50%, estimated by double-difference hypocenter relocations [e.g. *Waldhauser and Ellsworth*, 2000] and using a crack model for the earthquake source,

$$r = \left(\frac{7M_0}{16\Delta\sigma} \right)^{\frac{1}{3}} \tag{1}$$

where the source radius, r, and moment, M_0 of an earthquake can be related, assuming circular ruptures [*Eshelby*, 1957]. We assume the stress drop, $\Delta\sigma = 3$ MPa. We estimate the moment from an empirical relationship,

$$\log(M_0) = 1.6M_p + 15.8 \tag{2}$$

that relates M_0 to the NCSN preferred magnitude, M_p [*Wyss et al.*, 2004; *Turner et al.*, 2013].

As all of the RE candidate magnitudes are relatively small (i.e. $M_p < 3$, and in most cases $1 < M_p \leq 2$), and as most of our study region has sparse station coverage, we avoid using absolute travel times in our event relocations, as these may be affected by station clock errors [e.g. *Rubin*, 2002] or errors in event origin times. To avoid these issues, we adopt the approach of *Chen et al.* [2008], where S–P time is used to relocate seismic events instead of direct P- and S-phase arrival picks. In this method, the relative times for P and S (tt_p and tt_s, respectively) are derived from the S–P time and an assumed ratio of P-wave and S-wave velocities (V_p and V_s, respectively) via the relations,

$$tt_p = \frac{S_m P}{((V_p/V_s) - 1)} \tag{3}$$

and

$$tt_s = \frac{-S_m P}{(1 - (V_s/V_p))} \tag{4}$$

where $S_m P$ is S–P time. For more information about this method see *Chen et al.* [2008].

In order to use Equations 3 and 4 for relative relocations of our RE candidates using the HYPODD code [*Waldhauser and Ellsworth*, 2000] we need to have a precise estimate of differential S-P times with sufficiently high precision for relocating small events (e.g. of the order of milliseconds for $M_p = 1$). Data from NCSN stations (Figures S1 and S3), mostly have sample rates of 100 samples/sec. This sample rate allows for a 0.01 second precision time lag calculation using the time domain cross-correlation function. This degree of precision is inadequate for resolving the source separation that we require, which is of the order of 10 m.

To obtain the required precision, we measure differential S–P travel times using the cross-spectral method of *Poupinet et al.* [1984]. Delay times are estimated from the phases of cross spectra in a frequency band of 1–20 Hz with squared coherency of greater than 0.88, at a precision of 0.001 s (Figure S5). We prefer the cross-spectral technique over methods that employ polynomial or spline interpolation in the time domain [e.g. *Schaff et al.*, 2004; *Chen et al.*, 2008], since our tests suggest that time domain methods underestimate the lag

times with respect to the cross-spectral method (Figure S6); in addition, the cross spectral technique avoids errors from interpolation and curve fitting.

In order to calculate precise differential S–P times for a pair of events using the cross-spectral method, we first select 1 s time windows around the P and S arrival phases in each waveform. If the S-wave onset is unclear, we use a 1 s time window centered on the peak of S-wave energy [e.g. *Schaff et al.*, 2004]. The process of picking P- and S-wave arrivals is based on visual inspection, however, we use two different methods to help the user pick the arrivals or the centroids of the P- and S-waves – the first uses the event location with respect to the station and an assumed average velocity model to predict arrival times, and the second applies a moving cross-correlation of a 1-second window. For the latter method, the CCC of windows containing the P or S arrivals is typically higher than the values obtained for their codas. These two tools are very useful for choosing appropriate windows for cross-spectral analysis, especially for the S-wave arrivals that, in some cases, are not easy to pick visually.

1.5 Precise relative relocations

We next use the HYPODD code [*Waldhauser and Ellsworth*, 2000] and the methodology of *Chen et al.* [2008] to estimate precise relative locations for our candidate RE families. In this procedure, we use the precise S-P times, as estimated above, as well as the 1D velocity model provided for this area with the HYPO2000 code [*Klein*, 2014]. We then perform the double-difference relocation procedure for each candidate family separately; this avoids inaccuracies that may arise from including connections that have low CCC values (Figure S7). Note that in our relocation procedure there are no human-picked 'absolute' phase arrivals, just precise relative S–P times, estimated by cross-spectral analysis. These should be independent of any station clock errors or biases (Figure 3 in the main text).

1.6 Calibrating RE moment and recurrence to estimate creep rate

In Figure S10, we compare creep rates estimated from our RE data using four different calibrations. In each case, the values of the parameters α and β, as defined in Equation 1, are different. Hereafter, we refer to these calibrations as 'Nad98' [*Nadeau and Johnson*, 1998, $\alpha = -2.35, \beta = 0.17$], 'Nad04' [*Nadeau and McEvilly*, 2004, $\alpha = -1.09, \beta = 0.102$], 'Khosh' [*Khoshmanesh et al.*, 2015, $\alpha = -1.56, \beta = 0.10$] and 'SSF' (this study, $\alpha = -2.86$, $\beta = 0.17$). As you can see despite using different parameter values, creep estimated using

Nad98 and Nad04 calibrations are similar (root-mean-squared – RMS – difference of 0.6 mm/yr). Creep estimated using the Khosh and SSF calibrations are also very similar to each other for our REs (RMS difference of 0.2 mm/yr).

The differences in calibration parameters between Nad98 and Nad04 and Khosh, which are all derived from studies of the creeping central San Andreas fault at Parkfield and have a number of RE sequences in common, likely arise from a number of factors. Nad98 and Nad04 differ in the upper magnitude bounds of the events used – Nad98 including events with $M > 3.5$ such as the 1937–1990 Stone Canyon events and Parkfield mainshocks, and Nad04 excluding such larger events; the slope of the relationship between moment and slip is used to estimate the β parameter, and different values are obtained from different ranges of event sizes. Both Nad98 and Nad04 use the same background creep rate (23 mm/yr) to estimate α for all REs, but obtain different values of α in each case, suggesting a tradeoff between α and β.

The Khosh study, similar to Nad04, only considers RE sequences at Parkfield (excluding Parkfield mainshock), and thus they obtain a similar β. In order to estimate α, they subdivide the REs into six different regions, each with different creep rates, based on a creep rate distibution inverted from geodetic data, and in so doing, obtain a different value of α to Nad04.

In this study, we use one shallow RE sequence [1.4 km depth, likely sampling the same creep signal as the geodetic study of *Jin and Funning*, 2017, Figure S11]. We use this to calibrate the α value from Equation 1, adopting the β from Nad98.

That in two different cases (Nad98 and Nad04; Khosh and SSF) we can obtain similar creep rates from different α and β calibration values, suggests that there are tradeoffs between those parameters, and that neither is uniquely determined. It is beyond the scope of this study to resolve this issue, but it certainly motivates further investigation.

Supplemental figures

Figures S1–S12 are found at the end of this document.

Supplemental tables

Data Set S1. Catalog of confirmed repeating earthquakes

ds01: This data set contains information on repeating earthquake families that have been validated by precise relocation of each event in the family.

Columns:

ID: NCSN catalog event IDs

NC_lon: NCSN catalog longitude

NC_lat: NCSN catalog latitude

NC_dep: NCSN catalog depth

NC_mag: NCSN catalog preferred magnitude

Start_time: NCSN catalog origin time

DD: Information after this label is retrieved from Double-difference Earthquake Catalog for Northern California [1984-2011; *Waldhauser and Schaff*, 2008]. If it is blank, there is no information provided in the DD catalog.

lon: DD longitude

lat: DD latitude

depth: DD depth

mag: DD magnitude

Data Set S2. Catalog of possible repeating earthquakes

ds02: Same as dataset ds01 but for possible repeating earthquakes families – whose events have high cross-correlation coefficients, but could not be valiated by precise relocations. Columns are the same as for ds01.

Data Set S3. Catalog of repeating earthquake pairs

ds03: Same as dataset ds01 but for repeating earthquake pairs. Columns are the same as for ds01.

Data Set S4. Estimated creep rates from confirmed repeating earthquakes

ds04: Estimated creep rates for confirmed repeating earthquake families. Locations are based on the relocated catalog of *Waldhauser and Schaff* [2008]. If none of the events in a

sequence is in the relocated catalog, we report the NSCN location. We suggest to use creep rates for REs with coefficient of variation of recurrence intervals ≤ 0.4.

Columns:

ID: NCSN catalog event IDs

lon: DD catalog longitude

lat: DD catalog latitude

dep: DD catalog depth

creep_rate: Estimated creep rate

COV: Coefficient of variation of recurrence intervals for each family

Data Set S5. Estimated creep rates from possible repeating earthquakes

ds05: Same as dataset ds04 but creep rates estimated from possible repeating earthquakes families – whose events have high cross-correlation coefficients, but could not be valiated by precise relocations. Columns are the same as for ds04.

References

Chen, K. H., R. M. Nadeau, and R.-J. Rau (2008), Characteristic repeating microearthquakes on an arc-continent collision boundary – the Chihshang fault of eastern Taiwan, *Earth Planet. Sci. Lett.*, *276*, 262–272, doi:10.1016/j.epsl.2008.09.021.

Eshelby, J. D. (1957), The determination of the elastic field of an ellipsoidal inclusion and related problems, *Phil. Trans. R. Soc. Lond. A*, *241*, 376–396.

Frémont, M.-J., and S. D. Malone (1987), High precision relative locations of earthquakes at Mount St. Helens, Washington, *J. Geophys. Res.*, *92*(B10), 10,223–10,236, doi: 10.1029/JB092iB10p10223.

Jin, L., and G. J. Funning (2017), Testing the inference of creep on the northern Rodgers Creek fault, California, using ascending and descending persistent scatterer InSAR data, *J. Geophys. Res.*, *122*, 2373–2389, doi:10.1002/2016JB013535.

Khoshmanesh, M., M. Shirzaei, and R. M. Nadeau (2015), TimeâĂŘdependent model of aseismic slip on the central San Andreas fault from InSAR time series and repeating earthquakes, *J. Geophys. Res.*, *120*, 6658–6679.

Klein, F. (2014), Hypoinverse, v 1.40, ftp://ehzftp.wr.usgs.gov/klein/hyp1.40, Last accessed 2019/03/07.

McFarland, F. S., J. J. Lienkaemper, and S. J. Caskey (2016), Data from theodolite measurements of creep rates on San Francisco Bay region faults, California, *Open File Rep. 2009-1119 v1.8*, U.S. Geol. Surv., Menlo Park, Calif.

Nadeau, R. M., and L. R. Johnson (1998), Seismological studies at Parkfield VI: Moment release rates and estimates of source parameters for small repeating earthquakes, *Bull. Seismol. Soc. Am.*, *267*, 790–804.

Nadeau, R. M., and T. V. McEvilly (2004), Periodic pulsing of characteristic microearthquakes on the San Andreas Fault, *Science*, *330*, 220–222, doi: 10.1126/science.1090353.

Poupinet, G., W. L. Ellsworth, and J. Frechet (1984), Monitoring velocity variations in the crust using earthquake doublets: an application to the Calaveras fault, California, *J. Geophys. Res.*, *89*, 5719–5731.

Rubin, A. M. (2002), Using repeating earthquakes to correct high-precision earthquake catalogs for time-dependent station delays, *Bull. Seismol. Soc. Am.*, *92*, 1647–1659.

Schaff, D. P., G. H. R. Bokelmann, W. L. Ellsworth, E. Zanzerkia, F. Waldhauser, and G. C. Beroza (2004), Optimizing correlation techniques for improved earthquake location, *Bull. Seismol. Soc. Am.*, *94*, 705–721.

Shakibay Senobari, N., G. J. Funning, E. Keogh, Y. Zhu, C. M. Yeh, Z. Zimmerman, and A. Mueen (2019), Super-Efficient Cross-Correlation (SEC-C): A fast matched filtering code suitable for desktop computers, *Seismol. Res. Lett.*, *90*, 322–334, doi: 10.1785/0220180122.

Turner, R. C., R. M. Nadeau, and R. Bürgmann (2013), Aseismic slip and fault interaction from repeating earthquakes in the loma prieta aftershock zone, *Geophys. Res. Lett.*, *40*, 1079–1083, doi:10.1002/grl.50212.

Waldhauser, F., and W. L. Ellsworth (2000), A double-difference earthquake location algorithm: Method and application to the northern Hayward fault, *Bull. Seismol. Soc. Am.*, *90*, 1353–1368.

Waldhauser, F., and D. P. Schaff (2008), Large-scale relocation of two decades of Northern California seismicity using cross-correlation and double-difference methods, *J. Geophys. Res.*, *113*, B08331, doi:10.1029/2007JB005479.

Wyss, M., C. G. Sammis, R. M. Nadeau, and S. Wiemer (2004), Fractal dimension and b-value on creeping and locked patches of the San Andreas fault near Parkfield, California, *Bull. Seismol. Soc. Am.*, *94*, 410–421, doi:10.1785/0120030054.

Xu, W., S. Wu, K. Materna, R. Nadeau, M. Floyd, G. Funning, E. Chaussard, C. W. Johnson, J. R. Murray, X. Ding, and R. Bürgmann (2018), Interseismic ground deformation and fault slip rates in the greater San Francisco Bay Area from two decades of space geodetic data, *J. Geophys. Res.*, *123*, 8095–8109, doi:10.1029/2018JB016004.

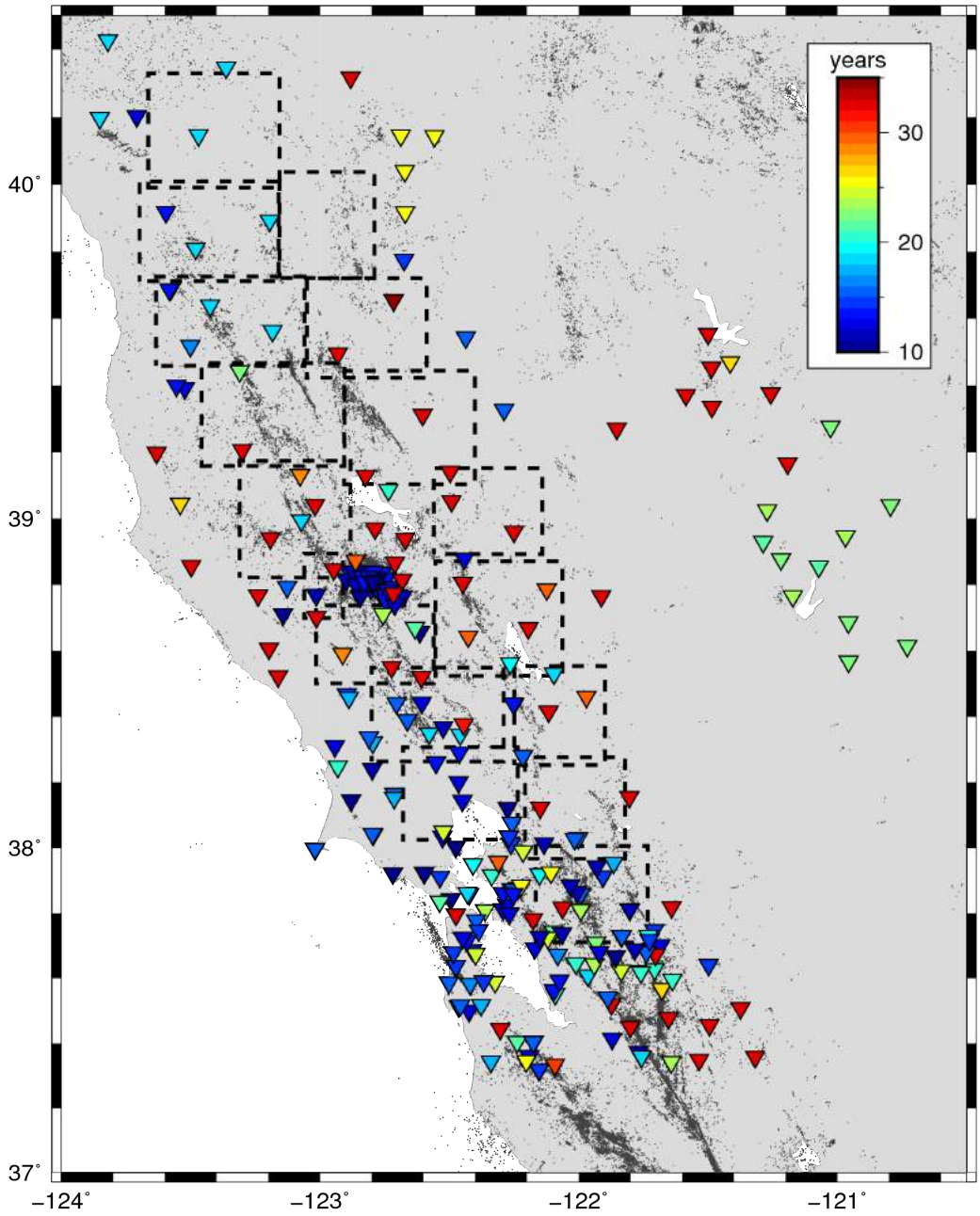

Figure S1. Station coverage and earthquake sampling subregions for the northern San Francisco Bay Area. Stations used in this study (inverted triangles) are color-coded by their total operating duration, between ~ 10 and 35 years. Subregions used for event selection are shown as dashed boxes. Gray dots are the locations of relocated seismicity.

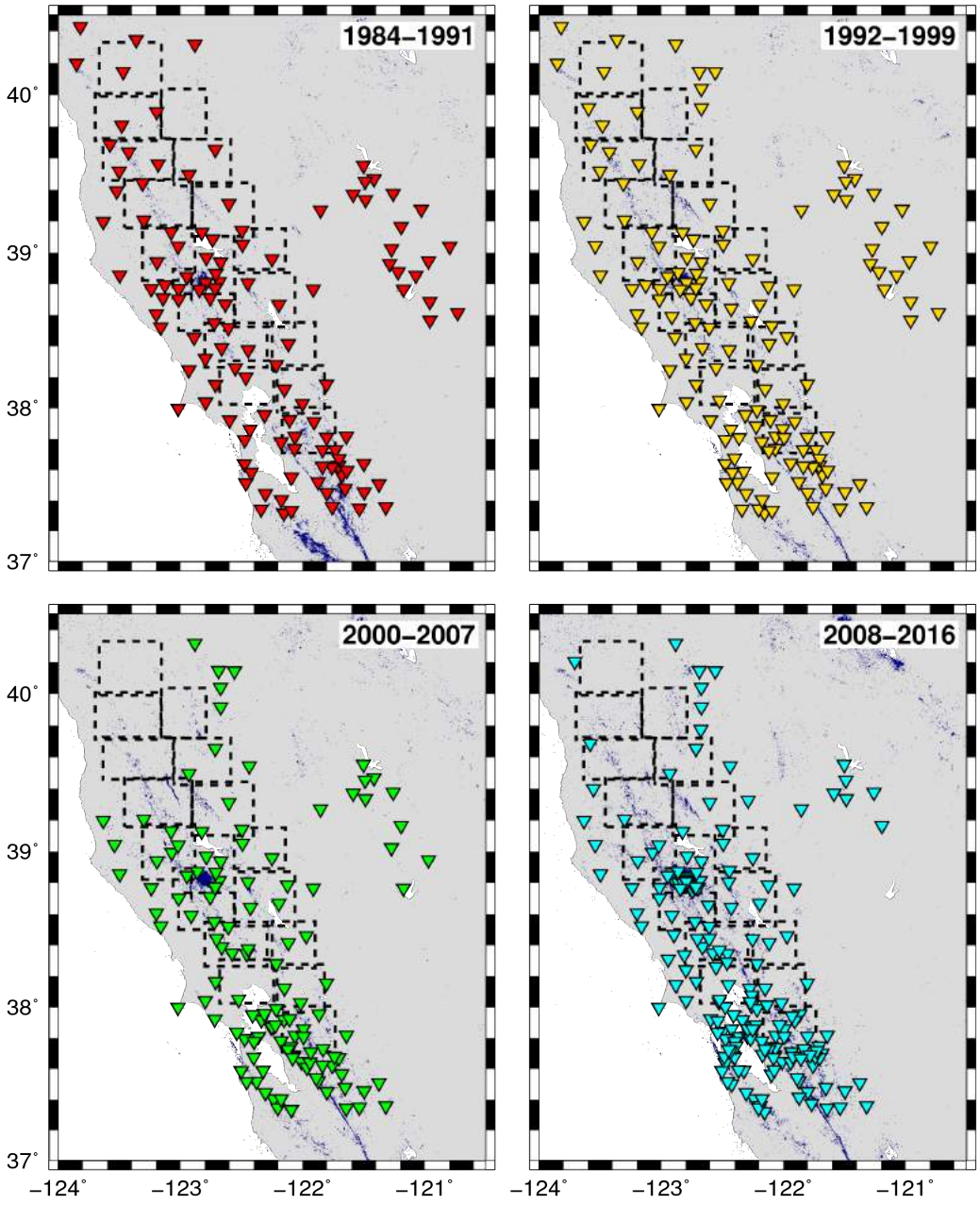

Figure S2. Evolution of station coverage in the northern San Francisco Bay Area over the period covered by this study (1984–2016). Stations are marked with inverted triangles, and subregions used for event selection are shown as dashed boxes. The configuration of the network changed significantly in the period of the study, particularly in the northwest portion of the study area, where there were very few stations operating between 2000 and 2007. Blue dots indicate locations of relocated seismicity in each period.

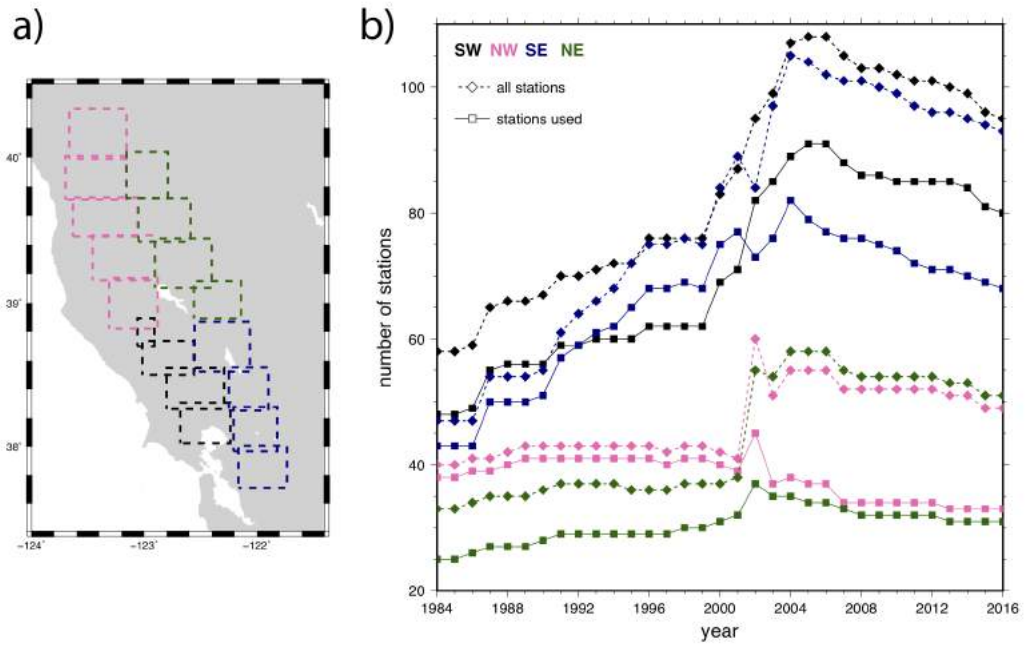

Figure S3. Station coverage as a function of time and position for this study. a) Location map showing earthquake subregions grouped together by fault – Rodgers Creek fault (black), Maacama fault (pink), Bartlett Springs fault (green) and Green Valley/West Napa faults (blue). b) Stations available for events in each fault group, per year. Two lines are shown for each group, indicating all stations available (dashed lines, diamond symbols), and stations used in this study (more than 100 detected events, solid lines, square symbols), color-coded as in a). Overall, fewer stations were available in the northern part of the region at all times, and we observe a major increase in available stations after ~ 2001, however this does not significantly increase the number of useful stations in the north.

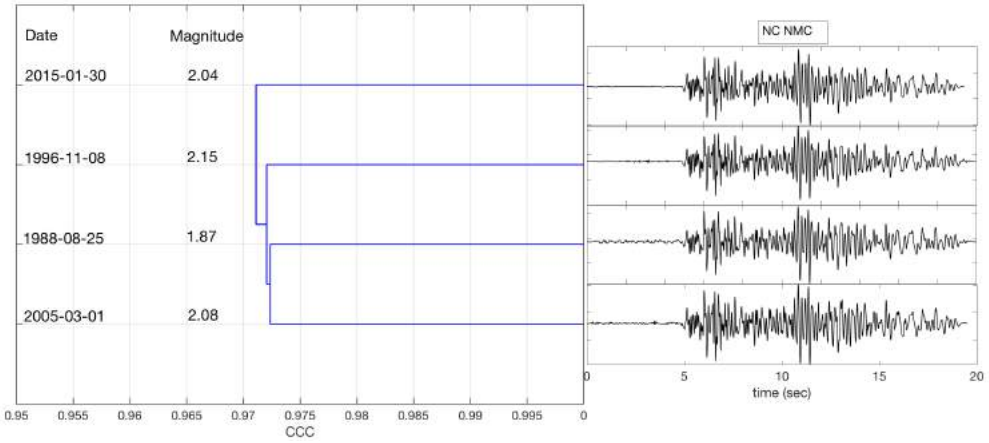

Figure S4. Example of a hierarchical dendrogram for an RE family detected on the central Maacama fault, northeast of Cloverdale. Corresponding seismic waveforms for these events recorded at station NMC are also shown. The similarity between events in this family from the average CCC matrix is greater than 0.97. This RE family is not connected to any nearby events, meaning that there were no other similar events to this family above our minimum CCC threshold of 0.8.

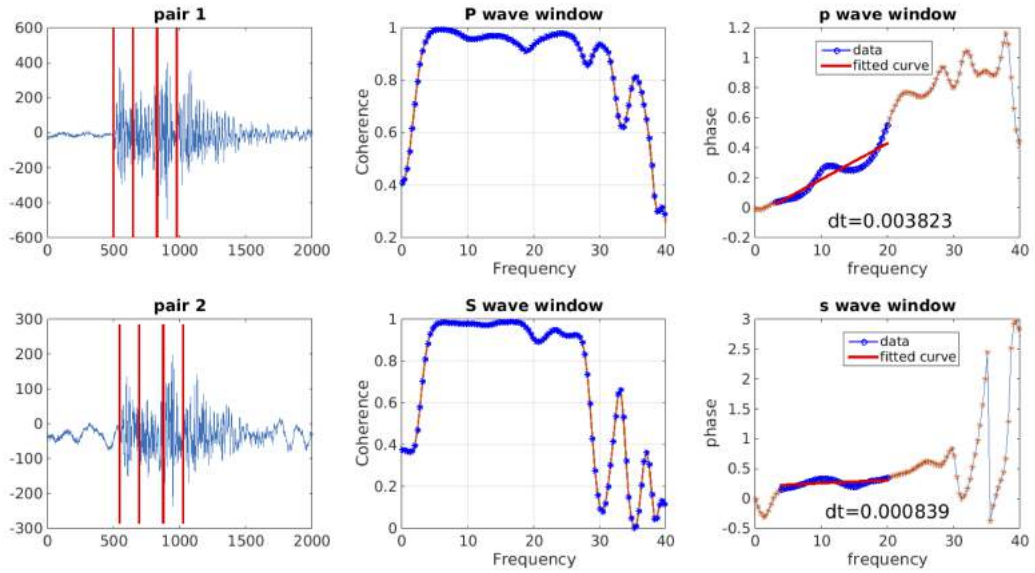

Figure S5. The cross-spectral approach for estimating relative S–P time for a pair of event waveforms. Left: We choose a one-second window starting with the P-wave and a second one-second window starting at the S-arrival or centered on the maximum S-wave amplitude if the S-arrival was not clear [e.g. *Schaff et al.*, 2004] for both events. Center: We estimate the delay times for both P- and S-waves based on calculating the best-fitting slope of the phase of the cross-spectrum plot versus frequency for the points with coherence above 88%. For more information about seismic delay time estimation based on the cross-spectral method see *Poupinet et al.* [1984] and also *Frémont and Malone* [1987]. Right: Finally, we take the difference between relative P and S delay times to estimate the S–P difference time for this pair – in this case, 0.003 seconds.

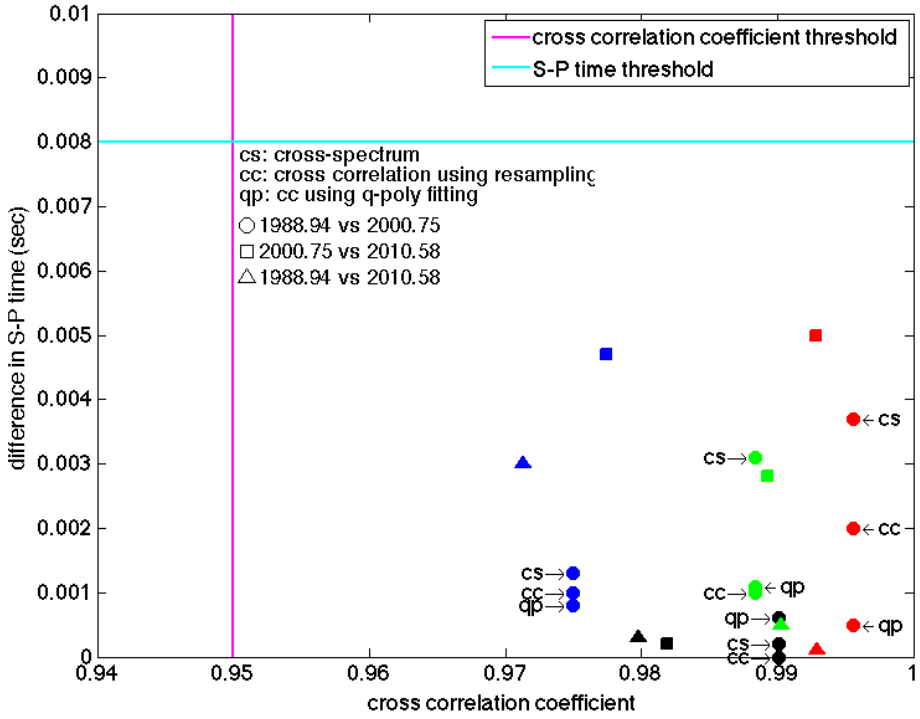

Figure S6. S–P time differences from multiple methods for all of the event pairs in a RE sequence (events as for Figure 3 in the main text). Results are color-coded by station (4 stations are shown). The cross-correlation coefficients for all pairs and all stations are greater than 0.97, greater than the commonly-used detection threshold of 0.95 [e.g. *Nadeau and Johnson*, 1998; *Chen et al.*, 2008]. Based on the magnitudes of these events, and assuming a back-azimuth of 45°, a stress drop of 3.0 MPa, and the velocity model of *Klein* [2014], we determine that 0.008 s is the maximum S–P time difference that could be indicative of a shared source. For event pair 1988.94–2000.75 we show results from three different estimation methods, the cross-spectral approach (cs), cross-correlation for interpolated waveforms (cc), and fitting a quadratic polynomial to the cross-correlation function (qp). For all of the pairs, methods and stations shown here, the differential S–P time is less than 0.006 s, implying that the earthquakes all share the same source region of the Rodgers Creek fault.

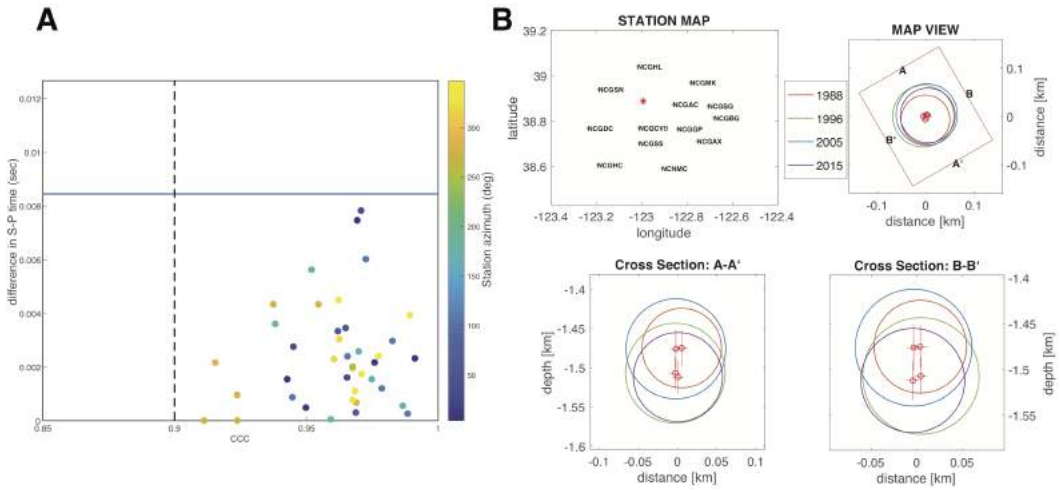

Figure S7. Validating RE families using precise event relocations. A) Differential S–P times plotted against cross-correlation coefficient, similar to Figure S6, for the RE family example shown in Figure S4. The S–P time is calculated by the cross-spectrum method and is plotted for all stations at a range of different azimuths (indicated by color scale) for each event pair in the family. B) Relative location for the same RE family after running HypoDD code. Red crosses and event-based color-coded circles indicate the errors of event locations and the dimensions corresponding to their magnitude assuming a 3 MPa constant stress drop source [after *Eshelby*, 1957]. We convert differential S–P times as shown in A) to relative P and S travel times using the method of *Chen et al.* [2008]. Note that as we are only interested in validating our RE candidates using their relative locations, we did not use any 'absolute' location information (e.g. individual picked phases), and therefore the absolute locations are not accurate. For validating RE family candidates we used B) as a filter and for RE pair candidates we use the results shown in A) as a location filter as it was not possible to relocate a pair of events.

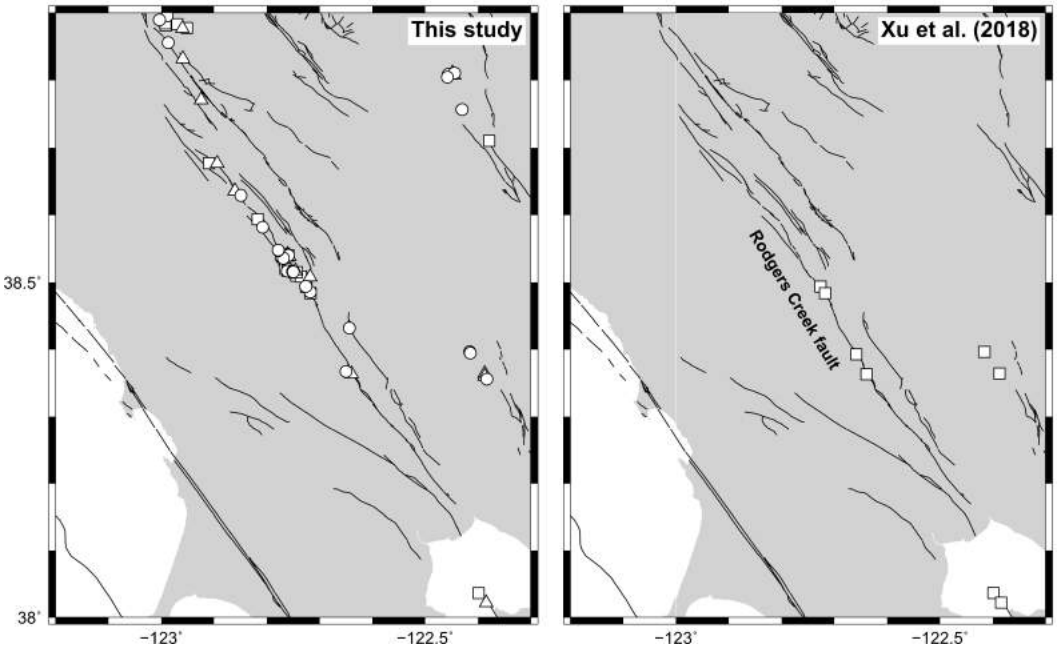

Figure S8. Comparison of densities of repeating earthquakes (REs) detected by different methods. Left: Results of this study, using a multi-station clustering approach. Along the Rodgers Creek fault zone (labeled) we identify 15 confirmed RE families (squares), 7 possible RE families (triangles) and 14 RE pairs (circles). These are plotted at their locations in the catalog of *Waldhauser and Schaff* [2008]. Right: Results of *Xu et al.* [2018], using long-lived stations. Four RE families are identified in total along the Rodgers Creek fault zone (squares). Multi-station clustering is more effective in this area at identifying REs.

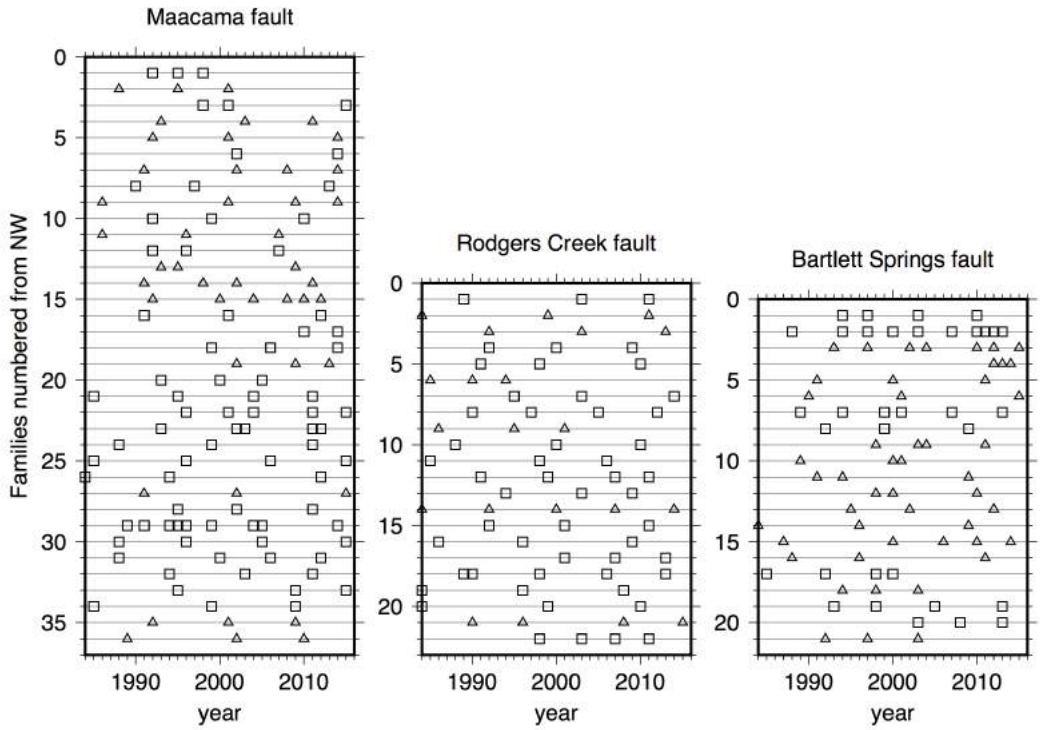

Figure S9. Temporal behavior of repeating earthquake (RE) families along three major fault zones in the northern San Francisco Bay Area. Confirmed REs (high cross-correlation events validated by precise relocation) are plotted as squares, possible REs (high cross-correlation events, not validated by precise relocation) are plotted as triangles.

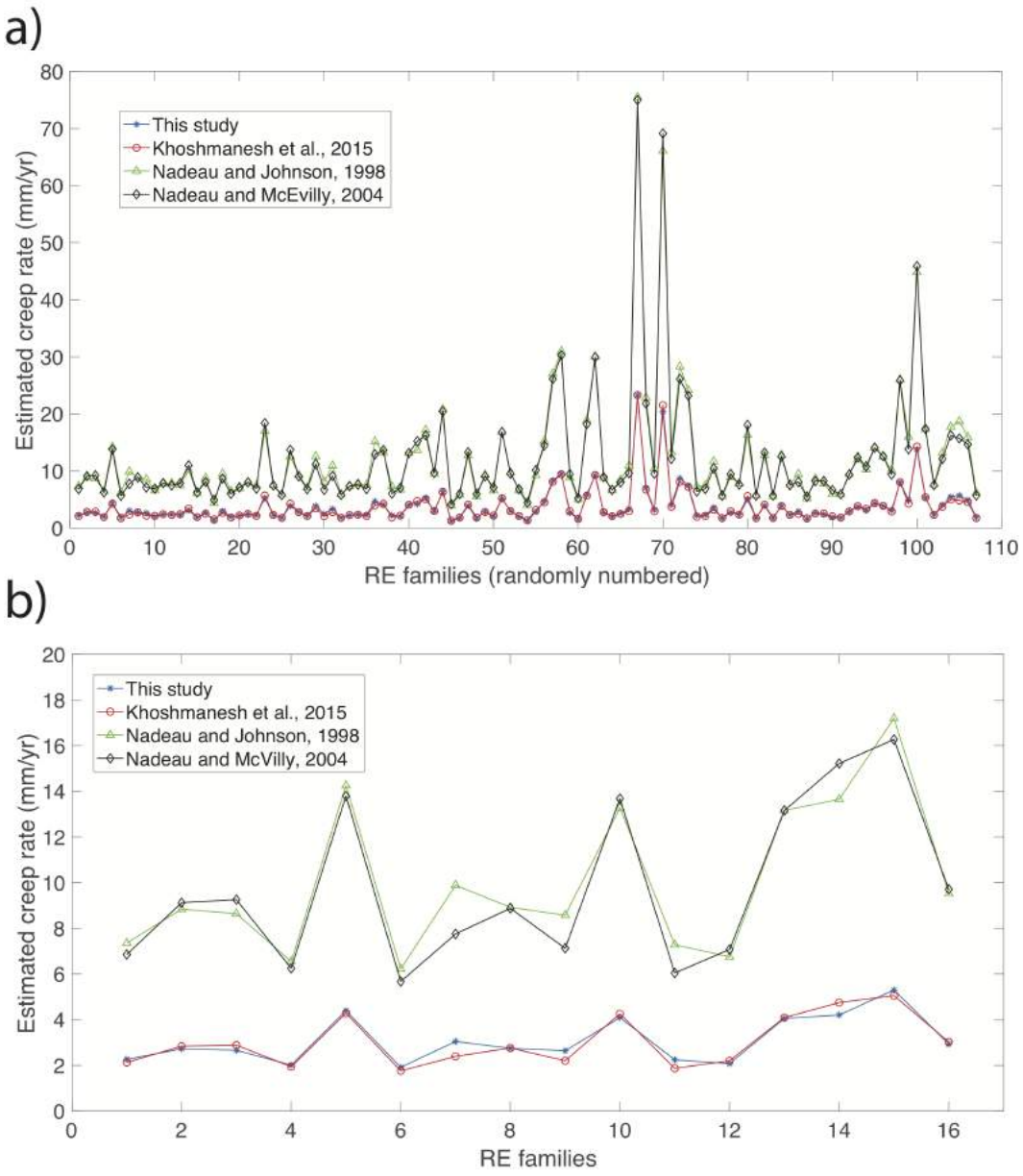

Figure S10. Estimated repeating earthquake (RE) creep rates using the calibrations of *Nadeau and Johnson* [1998], *Nadeau and McEvilly* [2004], *Khoshmanesh et al.* [2015] and this study for each confirmed RE family. We show plots for all REs we identify (a) and for only the REs on the Rodgers Creek fault (b). Despite using different scaling parameters α and β in each case, we find that the estimated creep rates fall into two groups that have very similar values – the calibration we obtain from this study gives a distribution of creep rates that is almost indistinguishable from that of *Khoshmanesh et al.* [2015], whereas the calibrations of *Nadeau and Johnson* [1998] and *Nadeau and McEvilly* [2004] result in creep rates that are 3.2 times faster.

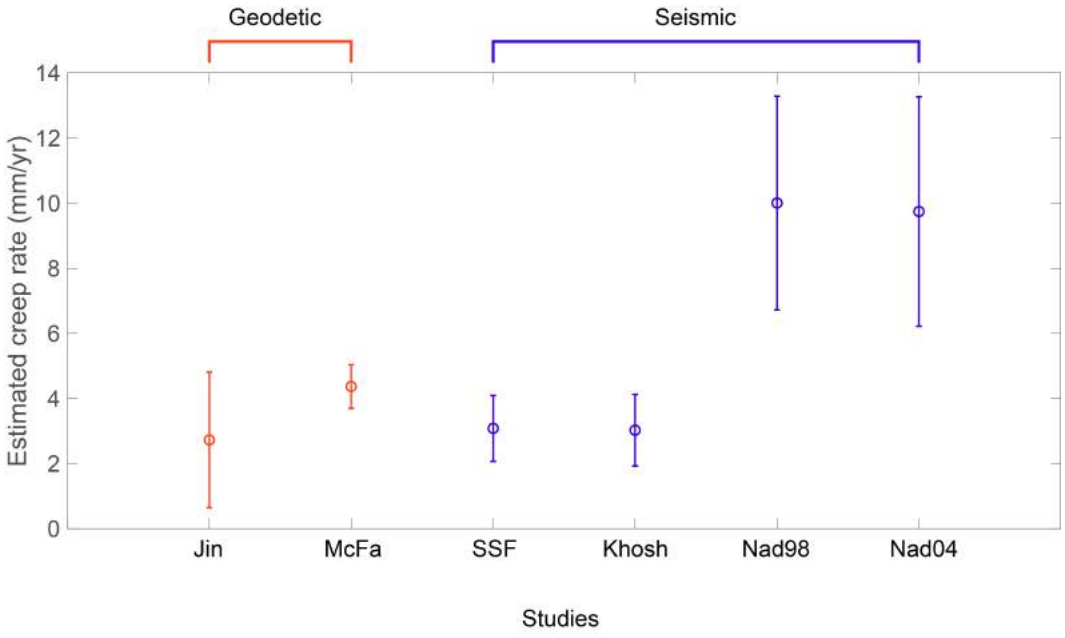

Figure S11. Comparisons of estimated creep rates for the Rodgers Creek fault. We compare creep rates from geodetic studies with those estimated 'seismically' using magnitudes and recurrences of our RE families under different calibrations. Two geodetic studies are shown [*Jin and Funning*, 2017; *McFarland et al.*, 2016, 'Jin' and 'McFa', respectively], and are broadly consistent with two of the seismic creep rates estimated using our calibration [this study, 'SSF'; *Khoshmanesh et al.*, 2015, 'Khosh']. As in Figure S10, the calibrations of *Nadeau and Johnson* [1998] and *Nadeau and McEvilly* [2004] give creep rates that are substantially higher than the others – 2–3 times higher than the geodetic rates for the Rodgers Creek fault.

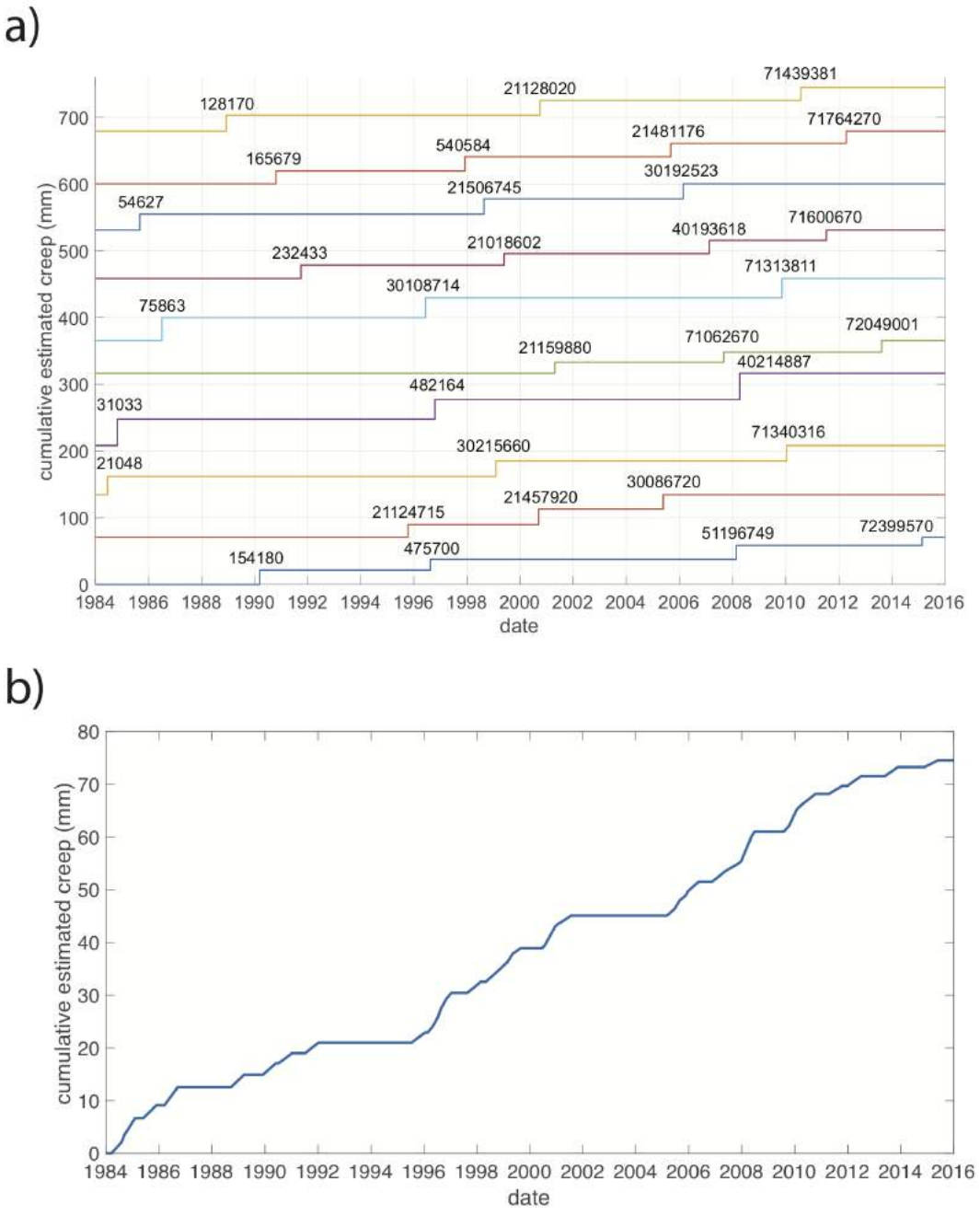

Figure S12. Cumulative creep (mm) over time for 10 families from the Rodgers Creek fault (Fig 4, Profile A9-B9). a) Estimated cumulative creep amounts (using the calibration from this study) are shown for each confirmed RE family sorted from bottom to top, based on location from south to north. b) The average cumulative creep estimated from all confirmed RE families. We smoothed the cumulative creep using a 0.5 year moving time window. There are two time windows, from 1992 to 1996, and 2002 to 2005, where we detect no REs and infer pauses in the creep.